5-1-2018

Roughness Based Passive Control Of Transition To Galloping Of A Circular Cylinder Undergoing Vortex Induced Vibrations

Kumar Swagat
Lehigh University, kumar.swagat@outlook.com

ROUGHNESS BASED PASSIVE CONTROL OF TRANSITION TO GALLOPING OF A CIRCULAR CYLINDER UNDERGOING VORTEX INDUCED VIBRATIONS

by

Kumar Swagat

A Thesis

Presented to the Graduate and Research Committee

of Lehigh University

in Candidacy for the Degree of

Master of Science

in

Mechanical Engineering

Lehigh University

May 2018

Certificate of Approval

This thesis is accepted and approved in partial fulfillment of the requirements for the Master of Science in Mechanical Engineering.

Roughness based passive control of transition to galloping of a circular cylinder undergoing vortex induced vibrations.
Kumar Swagat

_____

Date Approved

_____

Dr. Arindam Banerjee
Thesis Advisor & Associate Professor,
Department of Mechanical Engineering & Mechanics
Lehigh University

_____

Dr. Gary Harlow
Department Chair Person
Department of Mechanical Engineering & Mechanics
Lehigh University

Acknowledgements

I owe my deepest and profound gratitude to my thesis advisor, Dr. Arindam Banerjee, for his continuous guidance, moral support, and the opportunities that he has provided me with during my Master's research. I am truly grateful to Ashwin Vinod, who has been the pillar behind all the work I have been able to accomplish. He helped improve my understanding of flow induced motion and mentored me through every stage of my research. I would like to acknowledge Andrew Auvil for providing me with thorough insight into his Master's project and bringing me up to speed with performing experiments in the lab. I would also like to thank everyone from the lab: Pranav Modali, Angela Lawrence, Rinosh Polavarapu, Rahul Raghavendra, Sudharshan Kalidoss, Zack Farley, Erwin Fuentes and Aren Boyagi for their help and support. Finally, I must express my sincerest thank you to my parents, Rashmi and Debjeet Swain, whose love and support are always with me in every step of life.

Table of Contents

List of Figures

List of Tables

Abstract

Flow induced motion (FIM) is a naturally occurring fluid-structure interaction phenomenon, typically considered harmful to a wide variety of engineering structures. As a result, the majority of research in the field has been geared towards mitigating the occurrence of FIM. In 2005, Michael Bernitsas at the University of Michigan identified the energy harvesting potential of FIM's, triggering a new line of research that instead focuses on augmenting it. Previous work by our group had tested the effectiveness of strips attached to the surface of a circular cylinder in augmenting FIM modes such as vortex induced vibrations (VIV) and galloping. The objective of the experimental results presented in this thesis is to develop a better understanding of the effect of strip surface on the incitation of galloping oscillations. Strip roughness ratios (ratio of the size of embedded roughness to the total strip thickness) ranging from 0% (smooth surface) to 100% (rough surface with zero thickness) were tested in addition to strip thickness ratios (ratio of strip thickness to cylinder diameter) ranging from 0.8% to 8.2%. At the higher roughness ratios, rough strips led to suppression of VIV and galloping amplitudes when compared to their smooth counterparts. However, with decreasing roughness ratio and increasing thickness, the effect of surface roughness became negligible in comparison to the smooth surface. We conclude that beyond a threshold values of strip thickness, the mechanistic impact of the strip (thickness) is the dominant parameter affecting the cylinder's FIM response with no additional passive flow control possible by varying the surface roughness. At the lower threshold of thickness, neither the smooth nor the rough strips experienced galloping.

1 Introduction

1.1 Flow Induced Motion

Flow induced motion (FIM) is a phenomenon that depends on the field of engineering and system being considered. In this paper, FIM will be discussed in the context of fluid dynamics of the flow over bluff bodies. FIM can be categorized by the type of oscillator and source of excitation [1]. In general, the common types of FIM include vortex-induced vibration (VIV), galloping, buffeting, and flutter [2]. VIV and galloping are both examples of body oscillators caused due to flow separation in the wake of the bluff body. However, VIV is self-limiting as it is dependent on the wake behavior whereas galloping is not. Buffeting is caused by turbulence that leads to high-frequency oscillations of the body and is commonly experienced in civil engineering applications. Flutter is caused due to self-excitation of the body which occurs above a critical velocity that is dependent on the system's stiffness and damping. Flutter is a common issue in aerospace engineering, specifically in the design of airplane wings, as well as civil engineering structures. In this paper, the two types of FIM that will be in focus are VIV and galloping.

1.2 Vortex-Induced Vibration

Vortex-induced vibration (VIV) is a result of instability induced excitation due to the shedding of vortices from fluid separation around a bluff body. In the context of this paper, when flow separates over a cylinder, vortices are formed in the wake leading to a pressure differential on the surface of the cylinder. This pressure differential along with the asymmetric formation of vortices leads to alternating lift forces that oscillate the cylinder in a transverse direction to the flow. VIV of an oscillating, elastically mounted cylinder has

been widely studied. The response of a free, vibrating cylinder is dependent on various parameters, such as the mass and natural frequency of the system, the speed of flow and the Reynolds number regime. Reynolds number (*Re*) is a dimensional quantity, given by the ratio between inertial and viscous forces, which determines flow patterns under different conditions. For flow over a cylinder, Re is given by:

$$Re = \frac{UD}{\nu} \tag{1}$$

where U is the velocity of the flow, D is the outer diameter of the cylinder, and ν is the kinematic viscosity of the fluid. VIV of flow over a circular cylinder experiences changes in flow conditions from laminar to turbulent across different zones that take place over various Reynolds number regimes, which is why it is imperative to go over the specific Re regime of interest. Between laminar and turbulent states, there are three transition zones: TrW, TrSL, TrBL. Table 1.1 provides further details about each of these transition zones. Typically, the first transition for flow around a cylinder takes place in the wake, where laminar vortices are distorted causing them to become turbulent. The second transition occurs in the shear layers, with the transition zone moving upstream closer to the separation point of the flow. The third transition takes place around the separation point, causing the greatest impact on drag. The final and fourth transition occurs in the boundary layer, away from the separation point. The experiments discussed in this paper are primarily concerned with the TrSL2 regime, which spans $1.5\times10^3<Re<3\times10^5$ range.

From Figure 1.1, we can see how lift and drag forces on the surface of cylinder develop across various regimes of Re. C_D can be broken down into friction drag (C_{Df}) and pressure drag (C_{DP}). Friction drag is prevalent in laminar flows where viscous forces are dominant compared to inertial effects. With increase in Re, pressure drag becomes the

prominent component of the drag force. It can be seen from the figure that fluctuating lift force is always greater than the fluctuating drag force, which allows oscillation of the cylinder to take place.

At very low values of Re, the flow around a cylinder does not separate, and no vortices are formed. With a slight increase in Re, the flow starts to separate which lead to the formation of vortex pairs in the wake. In the range $40<Re<150$, the famous laminar Von Karman vortex street is observed. Apart from this mode, various other modes can be observed during VIV, as shown in Figure 1.2. Typically, the initial branch is characterized by 2S vortex shedding mode, where two single vortices are shed per cycle of oscillation [3]. Depending on system parameters, such as mass and damping, cylinders can undergo 2S, 2P or P+S shedding modes as well. Experiments have shown that the behavior and type of vortices formed in the wake vary depending on how close the system is to the lock-in regime, where the natural frequency and vortex shedding frequency overlap with each other. To calculate the frequency of vortex shedding, we use the Strouhal number (St), and it is defined as:

$$St = \frac{fD}{U} \tag{2}$$

where f is the vortex shedding frequency in Hz. For flows in the range of $3\times10^2<Re<2\times10^5$, St is approximately 0.2 [4]. During lock-in, where f is close to the natural frequency of the body, the phenomenon of resonance kicks in and the cylinder undergoes high amplitude oscillations which is known as “synchronization”.

Table 1.1 Various transition zones between laminar and turbulent flow states *(adapted from Zdravkovic, Flow Around Circular Cylinders: Volume 1:* Fundamentals (Oxford Science Publications, 1997[4]).

State	Regime	Re No. range	C_D
Laminar (L)	L1—No separation	0–4/5	↓
	L2—Closed Wake	4/5–30/48	↓
	L3—Periodic Wake	30/48–180/200	↑
Transition in wake (TrW)	TrW1—Far Wake	180/200–220/250	↑
	TrW2—Near Wake	220/250–350/400	↓
Transition in shear layer (TrSL)	TrSL1—Lower	350/400–1–2 × 10^3	↓
	TrSL2—Intermediate	1–2 × 10^3–2–4 × 10^4	↑
	TrSL3—Upper	2–4 × 10^4–1–2 × 10^5	↔
Transition in boundary layer (TrBL)	TrBL0—Pre-critical	1–2 × 10^5–3–3.4 × 10^5	↓
	TrBL1—Single Bubble	3–3.4 × 10^5–3.8–4 × 10^5	↓↓
	TrBL2—Two Bubble	3.8–4 × 10^5–0.5–1 × 10^6	↓↓
	TrBL3—Super-critical	0.5–1 × 10^6–3.5–6 × 10^6	↑
	TrBL4—Post-critical	3.5–6 × 10^6 to?	↔
Turbulent (T)	T1—Invariable	? to ∞	↔
	T2—Ultimate		?

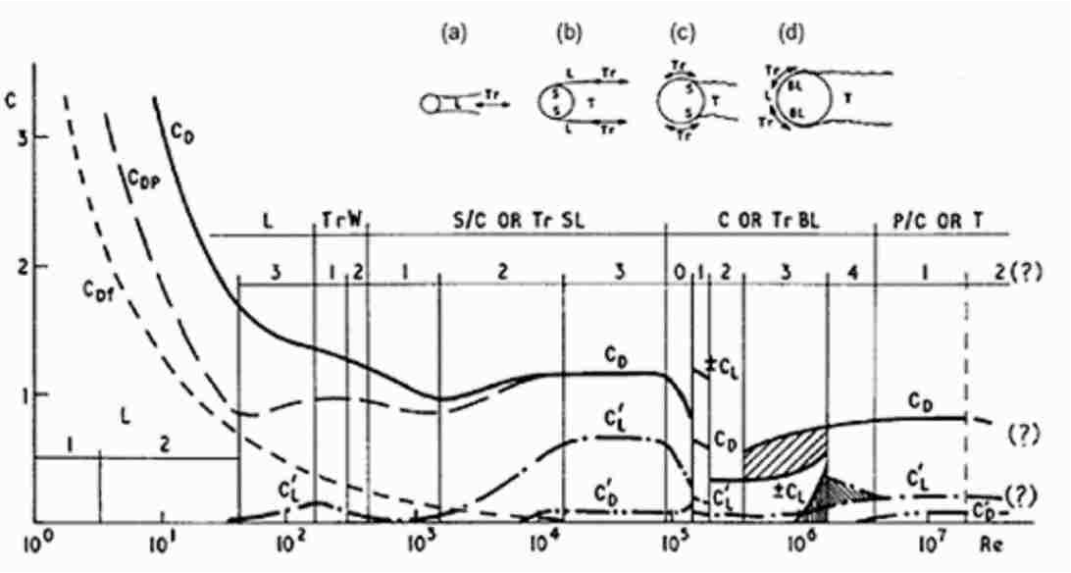

Figure 1.1 Lift and Drag coefficients versus Reynolds number *(adapted from Zdravkovic, Flow Around Circular Cylinders: Volume 1:* Fundamentals (Oxford Science Publications, 1997[4]).

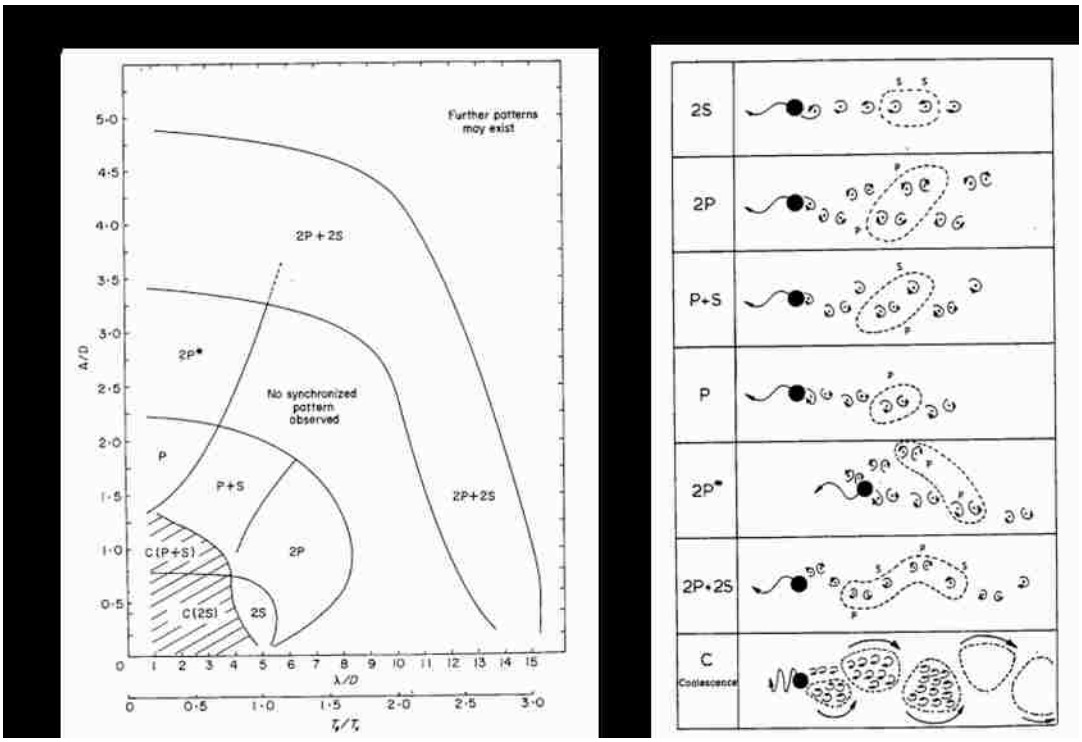

Figure 1.2 a) William-Roshko map for VIV; b) Various modes of vortex shedding during VIV [5]

1.3 Galloping

Galloping is a phenomenon that results from the asymmetry of the bluff body that is exposed to flow at high Reynolds number. It is characterized by high amplitude vibrations, much higher than what is observed for VIV. It is comparable to VIV as it is a result of flow separation. However, whereas VIV is self-limiting due to the effect of resonance, galloping is self-exciting and continues to grow in magnitude. This is a cause of concern, especially for engineering applications, as it can lead to structural damages. Since galloping arises due to the asymmetry of the body, any modification on the surface of the cylinder can lead to significant changes in lift and drag coefficients. A simple criterion is used to define galloping instability, known as the Glauert-Den Hartog criterion [6, 7]. It is defined as follows:

$$\left(\frac{dC_l}{d\alpha_l} + c_d\right)\Big|_{\alpha_l=\alpha} < 0 \tag{3}$$

where

$$C_l = \frac{2l}{\rho U^2 b} \tag{4}$$

$$C_d = \frac{2d}{\rho U^2 b} \tag{5}$$

where C_l is the lift coefficient, C_d is the drag coefficient, α is the angle of attack, l and d are aerodynamic forces, ρ is fluid density and b is characteristic length. From this criterion, we can conclude that a system is susceptible to galloping when this sum is negative or less than 0. It can also be seen from this equation that since asymmetry is crucial in exciting a system to gallop, a smooth cylinder will never experience galloping, irrespective of flow regime.

1.4 Mathematical Model

The elastically mounted smooth cylinder in water can be modeled as a spring-mass-damper system given by the second order linear equation [8]:

$$m\ddot{x} + c\dot{x} + kx = F(t) \tag{6}$$

where

$$c = 2\zeta\sqrt{m * k} \tag{7}$$

where x represents the direction of oscillation of the cylinder perpendicular to the flow, m is the total mass of the oscillating body and displaced fluid, c is the damping constant, and k is the spring stiffness. During VIV, F represents the alternating lift force F_l as a function of time due to flow separation. For the discussion of VIV and galloping of the cylinder in

this paper, mass and damping will be combined into a single mass-damping term that is defined as the product of the mass ratio m* and the damping ratio ζ.

Table 1.2 Non-dimensional parameters used in the work presented in the paper

Parameter	Symbol	Definition
Mass Ratio	m^*	$4m/\pi\rho D^2 L$
Damping Ratio	ζ	$c/2\sqrt{k(m+m_a)}$
Reduced Velocity	U^*	$U/f_n D$
Amplitude Ratio	A^*	A/D
Frequency Ratio	f^*	f/f_n
Reynolds Number	Re	UD/ν
Strouhal Number	St	Df_{vs}/U
Lift Coefficient	C_L	$2F_L/\rho U^2 D$
Drag Coefficient	C_D	$2F_D/\rho U^2 D$

Table 1.2 represents the various non-dimensional parameters that are typically used in the study of VIV response. Mass ratio (m*) is defined as the ratio of the total oscillating mass of the system to the mass of the displaced fluid and is a function of fluid density, outer diameter of the cylinder, and length of the cylinder. Damping is measured using the damping ratio, which is a ratio of the damping constant to the product of total mass and stiffness. It is calculated using the damping constant c, spring stiffness k, oscillating mass and added mass m_a. The added mass in the case of an oscillating cylinder is the displaced mass of fluid. The flow velocity U is non-dimensionalized to give reduced velocity by dividing by the diameter of the cylinder and natural frequency of the system f_n. Similarly, amplitude and frequency of oscillation are non-dimensionalized by dividing by the cylinder

diameter and natural frequency of the system respectively. Lift and drag coefficients are evaluated by measuring the lift and drag forces respectively.

1.5 Experimental Studies

The relevance of VIV in engineering applications has led to numerous research and experimental studies that date back to the late 90s, with extensive reviews by Sarpkaya [9, 10], Williamson and Govardhan [11], and Bearman [12]. Research experiments on galloping have also been performed to understand its behavior under different conditions. The following sections outline important work done by researchers around the world in these two areas of FIM.

1.5.1 Experiments on VIV

Khalak and Williamson [13] showed that for cases of low mass-damping, there exist three distinct branches in the amplitude response of VIV: initial, upper and lower. The initial branch occurs at low flow velocities, demonstrating random and unsteady low-amplitude vibrations. The upper branch occurs at slightly higher flow velocities. In this region, the frequency of vortex shedding frequency is approximately equal to the natural frequency, resulting in steady high-amplitude vibrations. The amplitudes in the upper branch have been observed to reach the order of one diameter for an elastically mounted cylinder. With further increase in flow velocities, the VIV response transitions into the lower branch. At this region, the vortex shedding frequency keeps increasing and is not equal to the natural frequency any longer, leading to low-amplitude vibrations that are not steady. Beyond this region, an increase in flow velocities leads to what is known as desynchronization. At this point, the response of the smooth cylinder shows sporadic oscillations with amplitudes much lower than those observed in the lower branch. Feng

carried out similar experiments but instead used a high mass-damping system. His results showed a different VIV response, with only an initial and lower branch. Figure 1.3 compares the results of both Williamson and Feng.

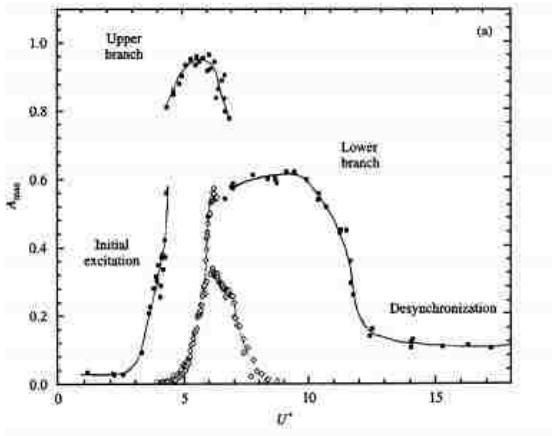

Figure 1.3 VIV response of a circular cylinder showing three distinct branches [13]

At the University of Michigan, Lee and Bernitsas [14] carried out experiments using a virtual c-k VIV model. An apparatus called the V_{CK} was designed to replace physical dampers and springs from the experimental apparatus with a motor-controller system that operated through a feedback loop. By doing this, they were able to easily vary damping and stiffness values using the control software. With this controller, they performed an extensive study on the response of VIV for varying damping at constant spring stiffness and varying stiffness and constant damping. Figure 1.4 a) shows experimental results for varying damping at constant stiffness case. The results of the study showed that increase in damping for a given stiffness led to a reduction in VIV amplitudes and reduction in the excitation range of reduced velocities. At higher values of stiffness, it was observed that the peak of the upper branch shifted to higher flow velocities. Therefore, higher damping was required to shift the peak back to lower flow velocities. This resulted in a more gradual transition to desynchronization. Figure 1.4 b) shows results for varying

stiffness at constant damping. We can see that as stiffness increase, the lock-in or synchronization regime is shifted to higher flow velocities. The width of the upper branch also shows an increase, spanning over a larger range of flow velocities. The maximum amplitudes in the upper branch also see an increase with increasing stiffness. With increasing spring stiffness, desynchronization starts to occur at a faster rate. It is imperative to note that although increase in stiffness does shift the response to higher Reynolds numbers, the occurrence of synchronization takes place at similar reduced velocity values irrespective of the value of spring stiffness.

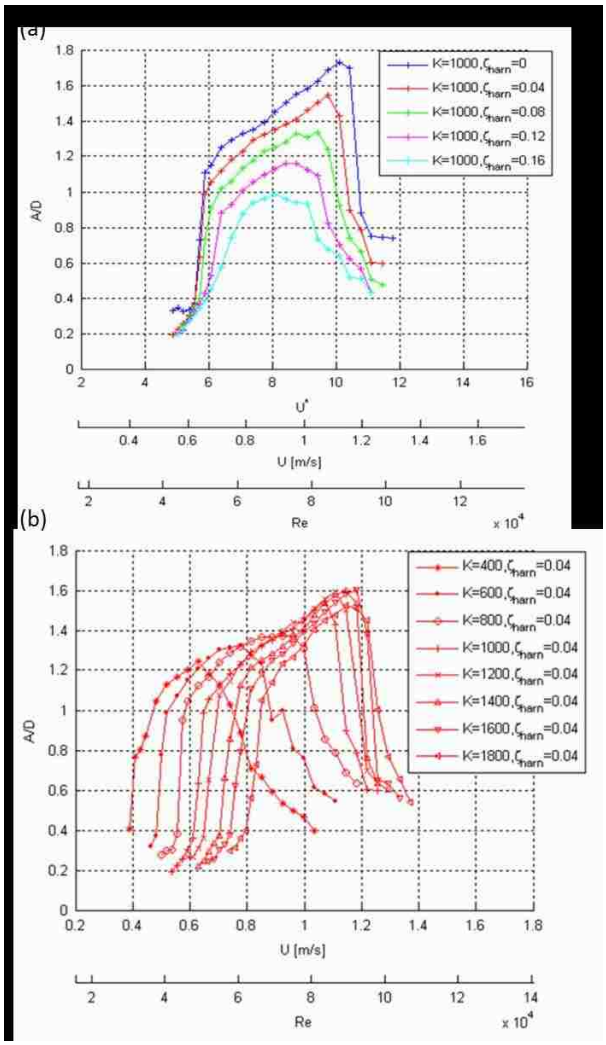

Figure 1.4 a) VIV response at constant stiffness and varying damping, b) VIV response at constant damping and varying stiffness [14]

The effect of Reynolds number was investigated by Raghavan and Bernitsas [15], which showed a strong effect on the VIV response of a circular cylinder. By making modifications to the size of the diameter of the cylinder, the study showed that the range of flow velocities corresponding to synchronization could be altered. This shift in synchronization can also be accomplished by changing the spring stiffness, which in turn leads to a change in natural frequency of the system. Over the years, the majority of research in the field of VIV has been focused with the TrSL2 regime, similar to the focus of this paper. Bernitsas and his group have conducted research in the TrSL3 regime, showing changes in the VIV response and underlining the importance of Reynolds number regime. They have shown that in the TrSL3 regime, the lower branch essentially ceases to exist, with a direct transition to desynchronization from the upper branch. In the TrSL2 regime, the upper branch is seen to have a round shape with a peak in amplitude, as shown in Figure 1.3. However, with increasing Reynolds number, the rounded shape of the upper branch starts to disappear and instead demonstrates a linear increase in amplitude with increasing width. The wake pattern during the initial branch for TrSL3 is also different from that observed in TrSL2, with the formation of 2P vortex shedding modes as opposed to 2S.

1.5.2 Experiments on Galloping

As galloping is majorly dependent on the asymmetry of the bluff body, several experiments have been performed to study the effect of modified surface geometries. Assi and Bearman [16] were able to excite circular cylinders to gallop by fitting different sizes of splitter plates on the cylinder's surface in the $1500<Re<16000$ regime. They studied the effect of varying plate lengths as well as plate porosity on the cylinder's response. The

study revealed that solid splitter plates were able to produce significant galloping responses, reaching displacement amplitudes 1.8 times the diameter of the cylinder at a reduced velocity of 8. Comparisons with VIV of a smooth cylinder showed that excitation regime was pushed to higher flow velocities for all tested cases. However, there was an increase in amplitudes as the velocities increased. PIV experiments visualizing the behavior of the wake showed that reattachment of the free shear layers on the plates was the cause of the galloping excitation.

Chang and Bernitsas [17] studied VIV and galloping responses of a circular cylinder using rough surfaces in the TrSL3 regime. In this study, Bernitsas' group refers to the use of rough strips as Passive Turbulence Control (PTC). According to the group, the application of PTC helps to trip the flow separation and energize the boundary layer. As a result, higher vorticity and lift forces can be generated leading to enhancement of the synchronization range and amplitudes of oscillation. The experiments focused on roughness location, coverage of surface and roughness level. Results showed that rough strips attached between 20° and 64° led to suppression of VIV and galloping oscillations. Moreover, galloping was not observed for strips attached at an angle greater than 64° and lower than 16°. Coarse, rough strips for a specific location did not show any prominent effect on VIV but led to increase in rate of galloping amplitudes. For a given grit size of roughness, strips attached between 16° and 64° led to higher VIV amplitudes along with increase rate of galloping.

Following the work with rough surfaces, Park and Bernitsas [18] carried out further investigation into PTC by studying localized surface roughness. Parallel strips relatively close to the boundary layer thickness were attached at various locations on the cylinder's

surface. Bernitsas' group developed PTC-to-FIM maps for P180 and P60 strips to present the effect on suppression and galloping. The map presented the various states of induced motion including weak suppression (WS), strong suppression (SS), soft galloping (SG) and hard galloping (HG) that were observed at different strip locations. The results from the study showed that there was a threshold of approximately one diameter before either of the hard galloping zones transitioned to galloping. HG1 experienced higher galloping amplitudes and spanned across a wider upper branch compared to HG2 for both P180 and P60 strips. Angles below 30° in the soft galloping zone showed a transition to galloping at lower values of reduced velocity. However, angles greater than 40° showed a delay in transition to galloping for increasing angle. Figure 1.5 shows the wake behavior that was observed for both soft and hard galloping using P180 and P60 strips respectively. All experimental cases resulted in suppression of amplitudes of the VIV response with higher harmonic frequencies.

Aside from surface modifications, various research studies have been performed to study different geometries of cylinders, particularly ones that are not circular. Nemes [19] changed the angle of attack of a square cylinder to study its effect on galloping. Tests showed that any orientation of the cylinder that resulted in it being symmetrical to the flow, such as a square or diamond orientations, did not gallop. However, with asymmetry, the cylinder exhibited mixed modes and resulted in galloping at lower oscillation frequencies. Manini [20] reviewed and performed galloping experiments using rectangular cylinders in a wind tunnel. He showed that a 3:2 aspect ratio was very susceptible to galloping instability. He observed high-amplitude vibrations for higher damping values and lower wind speeds as well. Alonso [6, 7] studied rhomboidal, biconvex and elliptical cross-

sections in wind at various angles of attack. Weaver [21] demonstrated soft and hard galloping for semicircular and parabolic cylinders.

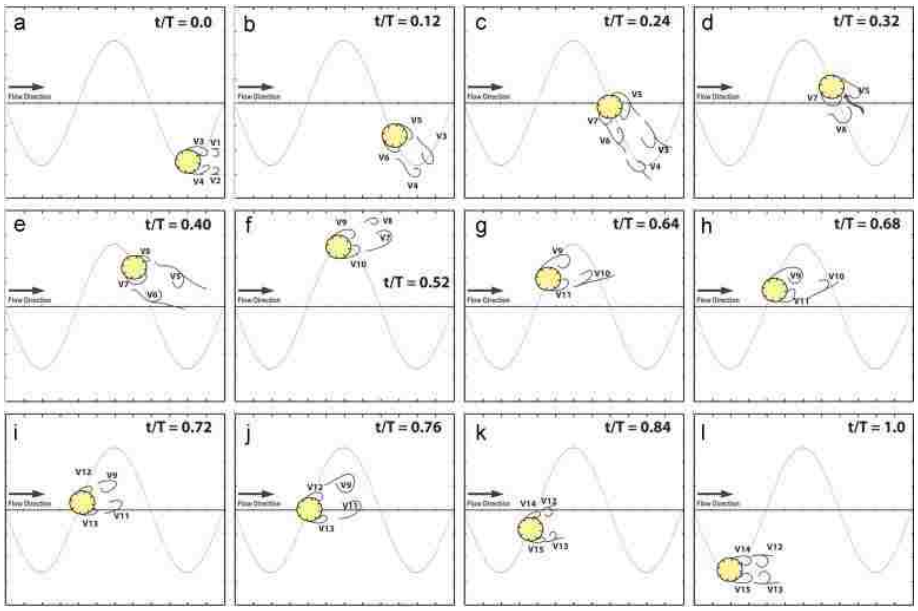

Figure 1.5 Wake vortex structures around rough cylinder during soft galloping [18]

1.6 Engineering Impact

Historically, VIV has held a negative stigma in the engineering world as it has been associated with numerous structural disasters. However, in recent years, interests in applying it in the field of energy harvesting has ignited its potential for growth. The following sections briefly discuss the various implications that VIV has on engineering fields along with its potential applications for power extraction.

1.6.1 Implications

VIV and galloping can have an adverse impact on civil, aerospace, mechanical, marine, offshore and nuclear engineering structures. The biggest example is the collapse of the Tacoma Bridge in Washington, which took place in 1940. The frequency of vortex shedding from the separated flow of wind over the bridge approached the natural frequency of the bridge structure, leading to high amplitude oscillations. This example shows why

design considerations with regards to natural frequencies of structures are of utmost importance. Similar situations that are not as well documented and large scale in nature face problems due to VIV and galloping on a daily basis. For example, ice formation on transmission lines can lead to high amplitude vibrations or the growth of sufficient marine organisms on oil risers can lead to galloping [22, 23]. Due to these implications, the majority of research in the field of FIM has been focused on identifying conditions that can prevent galloping from occurring and applying methods to suppress VIV to avoid failures such as cyclic loading of structures.

1.6.2 Applications

Renewable energy solutions are increasingly gaining awareness across the world due to the current and anticipated depletion rate of fossil fuels. In the last decade or so, R&D in industry and universities has seen an increase in the effort to derive energy from renewable sources. Apart from sources such as wind and solar, ocean energy poses huge potential for energy extraction. Reports show that available energy from ocean tides has the potential to meet 17 % of the world's energy demand [24]. As with any energy source, ocean energy also requires a mechanism for converting energy into usable power. Marine hydrokinetic energy (MHKE) is one such group of mechanisms that convert the kinetic energy from low head flows to mechanical work, which is then converted to electrical power that can be supplied to consumers via a grid. MHKE is usually divided into rotary devices, such as turbines, and non-rotary devices. Under the umbrella of non-rotary devices lies the application of vortex-induced vibrations. The following section briefly discusses details about the VIVACE converter.

1.6.3 VIVACE Converter

VIVACE, which is an acronym for Vortex Induced Vibrations for Aquatic Clean Energy, is a device that has been patented by Professor Michael Bernitsas and his group at the University of Michigan [14]. The device makes use of a bluff body, such as a circular cylinder, that is flexible to move through the use of elastic springs. With the flow of water over the cylinder, VIV is induced leading to high amplitude oscillations. Mechanical work of the oscillations is transmitted through a gear-belt system to a generator which converts the energy to electricity. Figure 1.6 presents a schematic of the VIVACE module that was developed by Bernitsas' group. Since this device can operate at low flow velocities, it can harness energy from the river and tidal currents that otherwise would be too slow for traditional energy harvesting mechanisms. Table 1.3 provides details about the theoretical and recoverable power from rivers in the United States that was published in 2012 by the Electric Power Research Institute [25]. The estimated values provided are based on turbine systems. However, since the majority of rivers have a flow speed of under 2 kn (1 m/s), it is not financially practical to use turbines. In contrast, synchronization range for VIV that can result in the conversion of energy to useful power can be achieved at flow velocities below 1 m/s, depending on the system parameters.

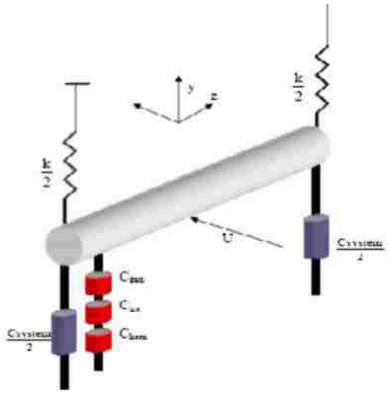

Figure 1.6 Simple schematic of VIVACE module at University of Michigan [14]

Table 1.3 Potential theoretical power available in rivers as reported by EPRI in 2012 [25]

Hydrologic Region	Theoretical Power (Annual Energy, TWh/yr)	Technically Recoverable Power (Annual Energy, TWh/yr)
New England	14.4	0.2
Mid-Atlantic	33.5	1.0
South Atlantic Gulf	38.5	1.2
Great Lakes	6.2	0.01
Ohio	79.2	6.9
Tennessee	20.4	1.0
Souris-Red-Rainy	1.8	0.03
Upper Mississippi	47.0	5.1
Lower Mississippi	208.8	57.4
Texas Gulf	8.9	0.05
Arkansas Red	45.1	1.3
Lower Missouri	79.8	5.6
Upper Missouri	74.3	2.8
Rio Grande	29.5	0.3
Lower Colorado	57.6	3.9
Upper Colorado	46.9	1.1
Great Basin	6.9	0
California	50.9	0.7
Pacific Northwest	296.7	11.0
Alaska	235	20.5
Total	1,381	119.9

1.7 Suppression Techniques of VIV and Galloping

As discussed earlier, VIV and galloping can be detrimental to a number of engineering fields. This has motivated researchers to come up with methods to negate the effects of both these phenomena's. Zdravkovich [26] did a comprehensive analysis of methods that modify the flow around a cylinder to suppress amplitude vibrations. These methods were divided into three categories depending on the type of feature modification used: surface protrusions, shrouds and near wake stabilizers. Surface protrusions, such as helical strakes, wires and fins, led to changes in the point of flow separation and behavior of separated shear layers. Different shrouds [27] were utilized to alter the entrainment layer

which prevented the growth of vortices in the wake region. Near wake stabilizers, such as sawtooth fins, splitter plates, and guide vanes, were shown to disengage entrainment layers from interacting with each other on either side of the cylinder.

Sui et al. [28] demonstrated significant suppression of the VIV response through the use of helical strakes. The experiments varied pitch angles, heights and surface coverage lengths of the strakes in order to study the effect on the cylinder's response. Strakes covering the entire length of the cylinder resulted in complete elimination of all three VIV branches. Additional strakes covering the cylinder also led to suppression by affecting the vortex structures, flow separation and interaction between free shear layers. A reduction in strake length showed suppression as well, but not to the extent of full coverage.

Experiments using localized roughness demonstrated mitigation of VIV amplitudes across flow velocities as shown by Park et al. [29]. Attachment of P180 rough strips at angles between $60° < \text{alpha} < 106°$ showed a reduction in peak amplitudes and a decrease in width of the lock-in regime. For zones that did not show strong suppression, the VIV response maintained a shape that was comparable to the smooth cylinder case with lowered values of amplitudes.

1.8 Augmentation Techniques of VIV and Galloping

Since the conceptualization of energy harvesting using underlying principles of VIV by Bernitsas' group, research in the field has extended to not just look at suppression mechanisms, but also study ways in which VIV can be amplified. Aside from work done by Bernitsas' group, Nakagawa et al. [30] performed tests at higher Reynolds number regime ($1x10^6<Re<6x10^6$) with wounded helical wires around a cylinder that resulted in

an increase of amplitudes by two times as compared to the smooth cylinder. Mahrenholtz and Bardowicks [31] observed maximum high amplitude oscillations in the subcritical regime by fitting fins symmetrically on the cylinder. Gartshore et al. [32] also carried out experiments with fins but tested it under both smooth and turbulent flow conditions. For turbulent conditions, amplitude oscillations of five times greater than that of the smooth cylinder was observed within the reduced velocity range of 4 and 6.

Vinod and Banerjee [33] performed extensive surface protrusion experiments with smooth and rough strips at different angles from the frontal stagnation point. All experiments were performed in the TrSL2 regime. P60 rough strips were tested at 60 deg, 80 deg, and 100 deg. Experiments at this roughness level showed highest amplitude oscillations at 60 degrees with a transition to galloping. The amplitudes observed in the upper branch were also higher than that of the smooth cylinder. Test cases of 80 deg and 100 deg showed suppression of VIV amplitudes and a decrease in synchronization range. Results for P36 and P320 at 60 deg showed increased VIV and galloping amplitudes as well. Experiments were also performed using smooth strips, which resulted in diminished amplitudes during VIV and a longer transition zone to galloping. However, the smooth strips resulted in much higher amplitudes for galloping at higher frequencies as compared to all levels of roughness tested. Figure 1.7 shows comparisons between the smooth and rough strip cases.

Following on the work with surface protrusion mechanisms, Auvil and Banerjee [34] carried out experiments by varying thickness of smooth strips at 60 degrees for different spring stiffness values in the TrSL2 regime. Results using the stiffest spring showed that with increasing thickness, there was an increase in the maximum allowable galloping amplitude at increasing rates of galloping. Moreover, the transition to galloping shifted to lower reduced velocities as well as a tendency of direct transition from VIV to galloping for increasing strip thickness. With increase in mass-damping at lower stiffness values, reduced amplitudes were observed for VIV. However, amplitudes in the galloping branch increased at higher rates, reaching higher amplitudes of vibration at lower flow velocities. Figure 1.8 provides results of increasing smooth strip thickness at low mass-damping.

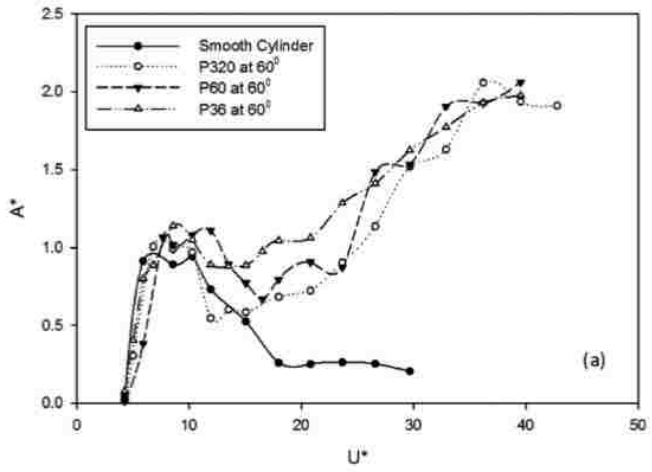

Figure 1.7 Comparison of *A** vs U* for smooth and rough strips at 60° [33]

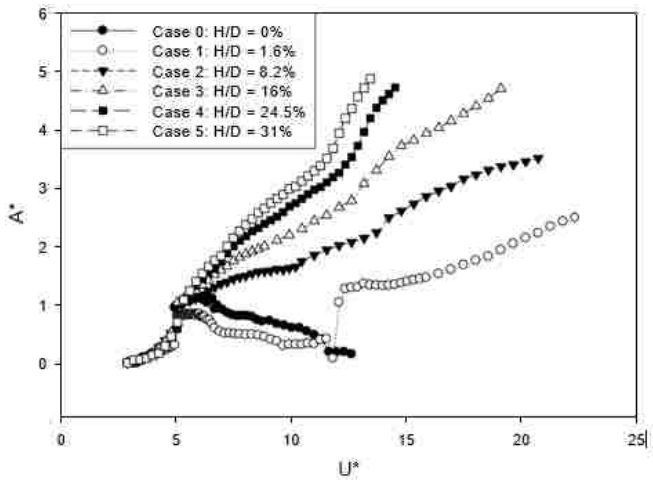

Figure 1.8 *A** vs U* for increasing thickness of smooth strips at 60° [34]

1.9 Motivation

The research presented in this paper is motivated to provide a further understanding of mechanisms that lead to suppression versus augmentation of VIV and galloping responses of a circular cylinder. The body of work presented primarily builds on prior research done by Vinod and Banerjee [33] as well as Auvil and Banerjee [34]. Vinod and Banerjee[33] showed that the optimum location for attaching strips on the surface of the cylinder in the TrSL2 regime in order to augment VIV and galloping response was 60 degrees from the frontal stagnation point. Moreover, they showed that at comparable thickness, smooth strips resulted in higher galloping amplitudes than rough strips. Auvil et al [34] studied the effects of smooth strip thickness on galloping of a circular cylinder and found that strip thickness not only increased the galloping oscillations, but also incited galloping at much lower flow velocities. The current work builds on previous experiments performed by our group, and aims to further identify the mechanism responsible for differentiating the characteristics of galloping oscillations observed in case of a circular cylinder attached with rough and smooth strips.

2 Methods

2.1 Apparatus

All experiments were performed in Lehigh University's Model No. 505 Water Tunnel, which was purchased from Engineering Laboratory Design in Minnesota. The test section measures 24'' x 24'' x 79'' (0.61 m x 0.61 m x 2 m) and is capable of generating flow speeds up to 0.95 m/s. Structural constraints which led to flutter at the free end of the cylinder enforced a limit on the maximum allowable flow speed for all experiments of 0.67 m/s.

Figure 2.1 shows a schematic of the experimental apparatus, drafted in SolidWorks by Andrew Auvil. The setup allows the cylinder to oscillate freely in transverse motion to the direction of flow. The cylinder is screwed in place to the bottom of the acrylic plate using a 3/8'' diameter screw. The acrylic plate itself is supported by air bearings from NewWay Inc. The air bearings are an expensive piece of the overall apparatus. The air bearings move along the steel shafts and are provided with compressed air at a pressure of 80 psi through a compressed air supply line. Another acrylic plate is attached on top of the air bearings and is used to mount the LVDT body. The LVDT has been a new addition to the overall apparatus, before which cameras were used to record displacement of the cylinder. The core rod of the LVDT is held in place using #4-40 threaded rods, which are screwed into either end of the core rod and extend outwards from the LVDT. The extended threaded rods are mounted using L brackets that are positioned on a slotted steel strut at both ends. The slots are provided so that the position of the L brackets can be adjusted horizontally and vertically in order to align the threaded rods. The attached core rod and threaded rod system is pulled taut and tightened carefully at the L brackets to ensure there

is no friction between the core rod and inner body of the LVDT. Appendix A and B provide more information on tuning the system for damping tests and standard procedures to be followed prior to running each experiment. Springs of varying stiffness values are attached to the setup with the help of hooks on slotted angle steel struts. It is imperative to incorporate the elastic springs as they help categorize the experiment through a quantifiable stiffness value and model resistance to vibration that would otherwise be provided by the fluid in a real-world engineering application.

A circular cylinder made out of PVC pipe that measures 22'' (0.762 m) in length and 1.9'' (0.0483 m) in diameter was used for all experiments. With a tunnel width of 24'' (0.61 m), the blockage ratio is 7.9 %. This is below the threshold of 14%, above which blockage can have a considerable impact on the VIV and galloping response.

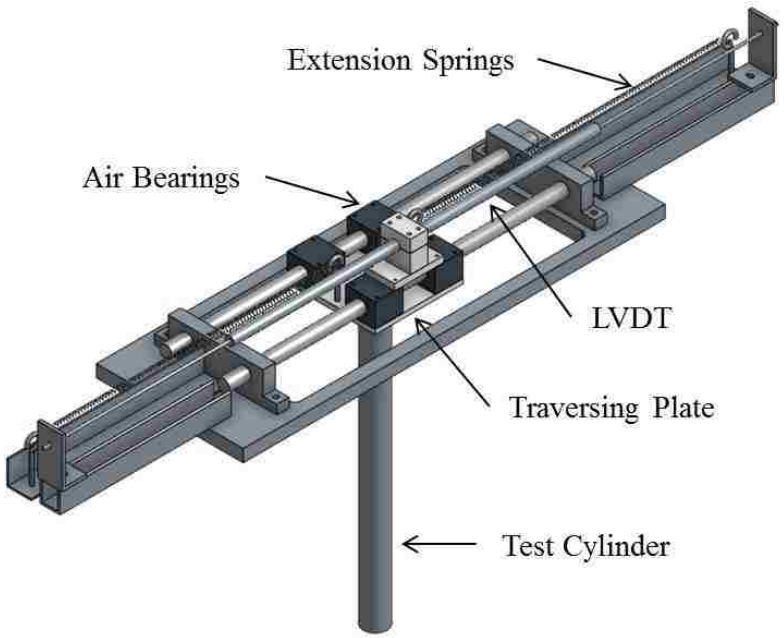

Figure 2.1 CAD model of experimental apparatus [34]

2.2 Diagnostics

A linear variable differential transformer (LVDT) from TE Connectivity's SE750-20000-200 series was used to record the displacement of the cylinder. This model of the LVDT has a linearity error of 0.10% of the full-scale output, which corresponds to ± 0.02 inches. The cylinder's oscillations move the LVDT body, producing a change in magnetic field that leads to the induction of EMF or voltage. The voltage reading is directly proportional to the displacement of the cylinder. The LVDT is wired to a digital acquisition system (DAQ) in order to transfer the voltage readings. A USB-6003 DAQ from National Instruments was used. The DAQ board is connected to the computer via USB cable. Data collected from the LVDT was processed on the computer using a LabVIEW script. This script was able to extract voltage readings from the DAQ and convert it into displacement readings using a linearity slope of 2. The LabVIEW VI monitored oscillations of the cylinder for two minutes at a frequency of 10 samples per second. The raw data was then saved in an excel file, which was post-processed using a MATLAB script. The MATLAB script is provided in Appendix E.1.

Damping tests were performed in air without the cylinder before running each experiment in order to maintain uniformity in the damping ratio (ζ). Appendix D provides details on how the system was tuned to achieve the desired damping ratio. For each damping test, the acrylic plate was pulled completely to one end of the tunnel and released to oscillate freely. The motion of the LVDT body was monitored using the LabVIEW script for 30 seconds. Figure 2.2 provides an example of the displacement trace of the system used for a damping trial. The raw data from the damping test was saved in an excel file, which was then processed using another MATLAB script. This MATLAB script is

provided in Appendix E.2. The logarithmic decrement method was used to calculate the damping ratio, as show below. Relevant equations used in the MATLAB script are provided below.

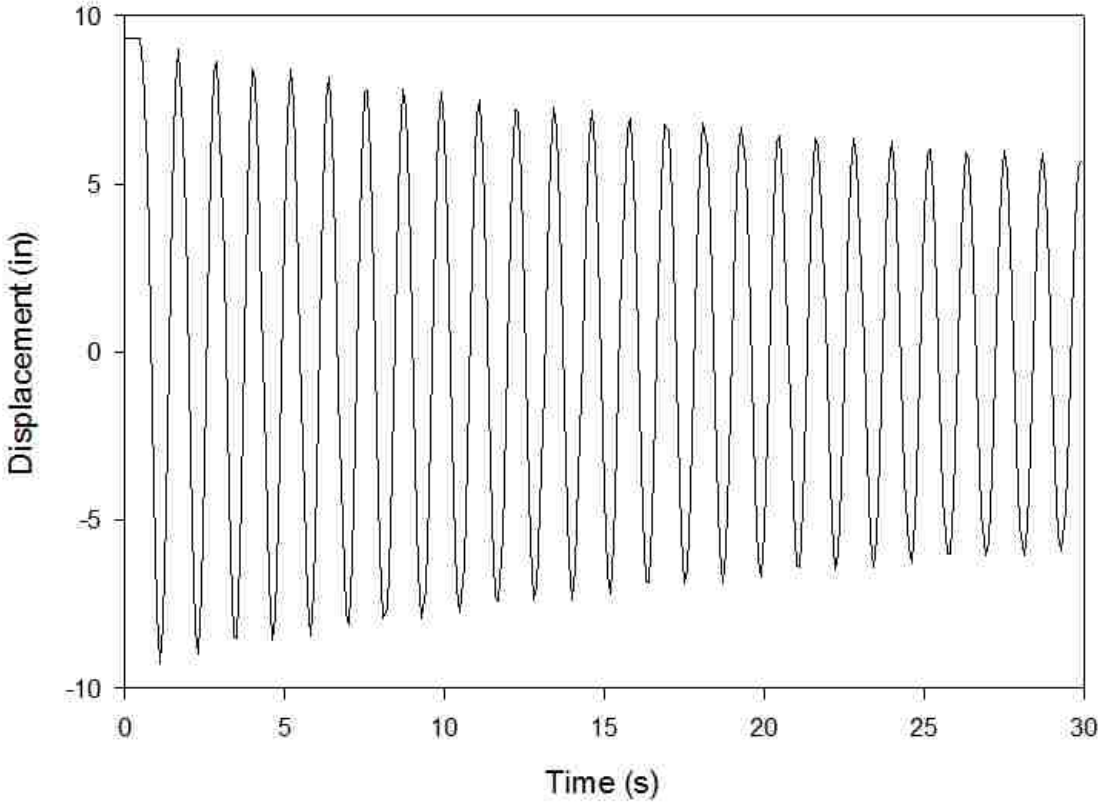

Figure 2.2 Displacement trace history for damping test of stiff spring

$$\delta = \frac{1}{n}\ln\left(\frac{x_0}{x_n}\right) \tag{8}$$

$$\zeta = \frac{\delta}{\sqrt{4\pi^2+\delta^2}} \tag{9}$$

$$\zeta = \frac{c}{2\sqrt{k(m+m_a)}} \tag{10}$$

where δ is the logarithmic decrement and n is the nth peak in the displacement trace.

2.3 Test Cases

One experimental parameter was varied in order to understand its effect on VIV and galloping response: roughness ratio. This ratio is defined as the thickness of the average grain size of a rough surface to the total strip thickness, as shown in Figure 2.3.

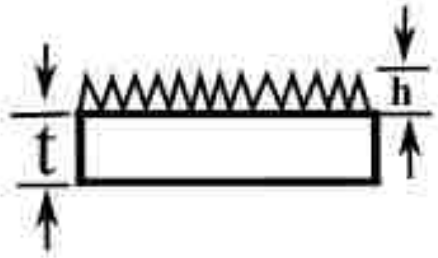

Figure 2.3 Cross sectional view of rough P60 attached on base strip

$$Roughness\ Ratio = \frac{Average\ grain\ size}{Total\ strip\ thickness} = \frac{h}{t+h} \tag{11}$$

P60 rough strips, measuring 864 μm (0.034'') and 0.0127 m (0.5'') in thickness and width respectively, were used for all the experiments. The strips were attached to the cylinder's surface at an angle of 60 degrees from the frontal stagnation point. As shown by Vinod and Banerjee [33], strips attached at a 60 degree separation proved to be the optimum orientation that leads to high amplitude galloping for a circular cylinder in the TrSL2 Reynolds number regime. Different tapes of varying sizes were used to vary the total strip thickness. Table 2.1 lists the different tapes used with their respective base thicknesses. For each case of the rough strip, corresponding experiments were performed with smooth tape strips, measuring 787 μm (0.031'') in thickness and 0.0127 m (0.5'') in width. For all experimental cases, irrespective of the type of surface used, the total thickness of strips was kept the same. All experiments were performed at the same damping value for the system.

A custom made, music wire spring from W.B. Jones Springs Inc. with a stiffness value of 81.4 N/m was used. The natural frequency, damping ratio and damping constant of the spring are listed in Table 2.2. The effect of 100 % roughness ratio was achieved by creating grooves on the cylinder surface at 60 degrees from the stagnation point. The rough strips were glued inside the grooves using E6000 adhesive. The depth of the grooves used was approximately is 0.02'', as shown in Figure 2.4. It is imperative to note that the rough strips were carefully attached to the surface of the cylinder. As the P60 strips are stiff, ample amount of force was applied to ensure no section of the strip along the length of the cylinder was left with gaps. The presence of gaps can lead to effective thickness, which can significantly alter the response of the cylinder at high roughness ratios. Fourteen total cases were tested, with seven cases for the rough strips and seven cases for the smooth strips. All the test cases are listed in Table 2.3.

Table 2.1 List of foam tapes used for varying total thickness

Tape Used (name)	**Base Thickness (mm)**
4926 3M adhesive	0.381 (0.015'')
4905 3M adhesive	0.508 (0.02'')
4646 3M adhesive	0.635 (0.025'')
Smooth strips	0.787 (0.031'')
	1.575 (0.062'')
	3.15 (0.124'')

Table 2.2 Stiff spring parameters

Spring Stiffness, k (N/m)	**Damping Ratio, ζ**	**Damping Constant, c**	**Natural Frequency, $f_n(Hz)$**
81.4	0.015	0.163	0.656

Table 2.3 Experimental Cases

Case #	Surface Type	Roughness Ratio (%)	H/D
1	P60 rough strips	100	0.8%
2		22.4	2.6%
3		20.3	2.8%
4		18.6	3.1%
5		16.9	3.4%
6		11.5	5.1%
7		6.9	8.3%
8	Smooth strips	0	0.8 %
9			2.4 %
10			2.7%
11			2.9%
12			3.3%
13			4.9%
14			8.2%

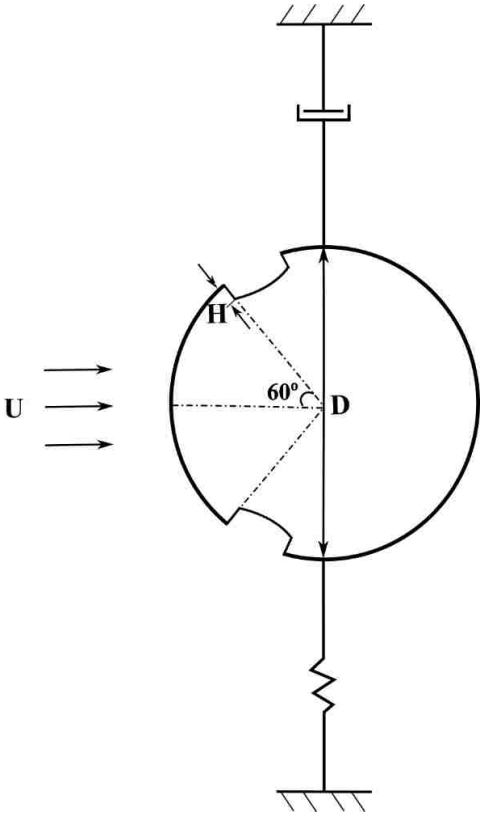

Figure 2.4 Top view of grooved cylinder exposed to flow

3 Results and Discussion

The following discussion is geared towards trends in VIV and galloping response with respect to changes in roughness ratio. In addition, comparisons are drawn between the effects of using the two different strip surfaces on the cylinder. All the observations are presented through an analysis of amplitude, displacement, dominant frequency and frequency spectra.

3.1 VIV response of a plain circular cylinder

It is imperative to first go over the VIV response of a plain circular cylinder. Tests were performed to validate previous results and damping of the system. Figure 3.1 represents the amplitude and frequency response of the plain cylinder across the entire range of tested U^* values. The cylinder demonstrated the three distinct initial, upper and lower branches. This is similar to the findings from the classical work of Khalak and Williamson [3]. Similar results for amplitudes across U^* were noted as compared to Auvil's work in the effect of strip thickness on flow induced motion of a circular cylinder [34]. The initial branch spanned across $2.9 < U^* < 4.9$. The upper branch was observed in between $5.0 < U^* < 6.3$, reaching a maximum A^* value of 1.1. Within this branch, the frequency of vortex shedding approached the natural frequency, resulting in f^* values of 1. As shown in Figure 3.2, f^* of 1 represents steady, high amplitude oscillations due to "synchronization" or "lock-in". The peak observed in the frequency spectrum is clearly dominant as well. From $6.4 < U^* < 10.7$, the cylinder remained in the lower branch where the amplitudes kept decreasing with increasing U^*. The f^* values slowly increased from 1 and remained constant at 1.2 for $U^* > 8.3$. Following the lower branch, the cylinder entered

the region of desynchronization, where low amplitudes and unstable oscillations were observed.

(a)

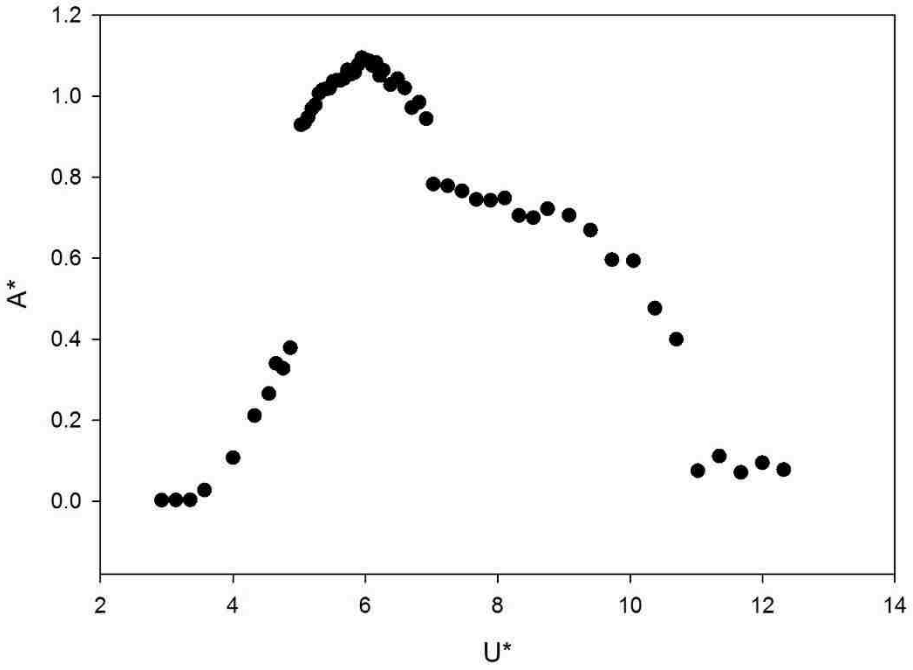

(b)

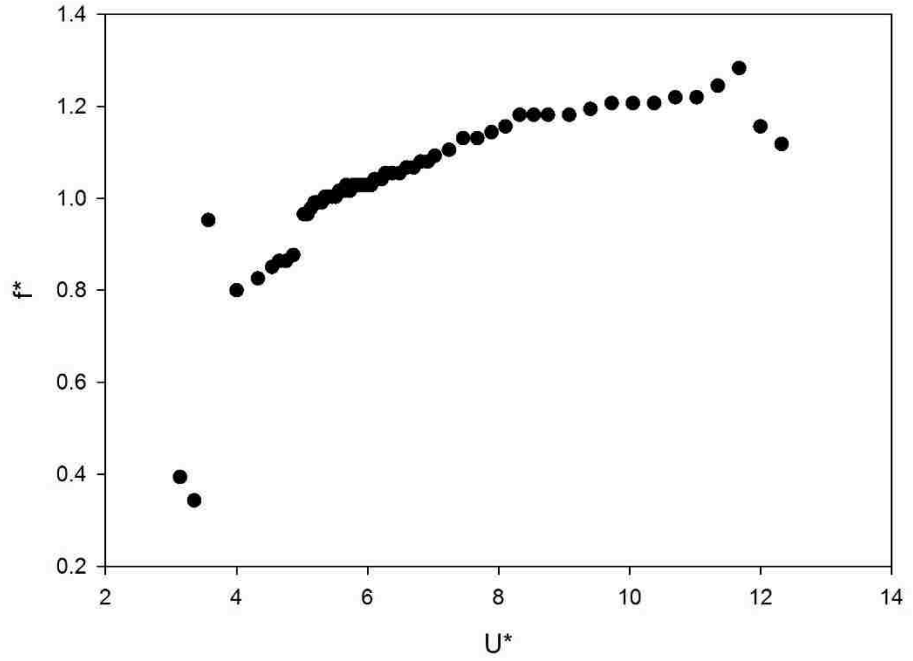

Figure 3.1 a) Vibrational amplitude and b) Oscillation frequency response of plain cylinder ($m^*\zeta = 0.015$)

(a)

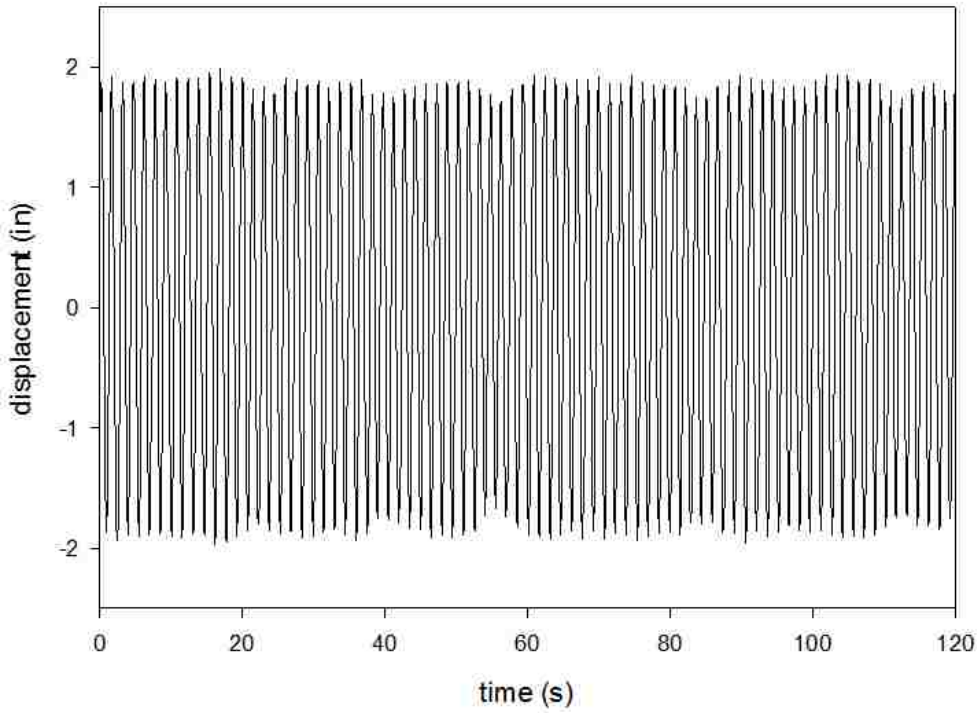

(b)

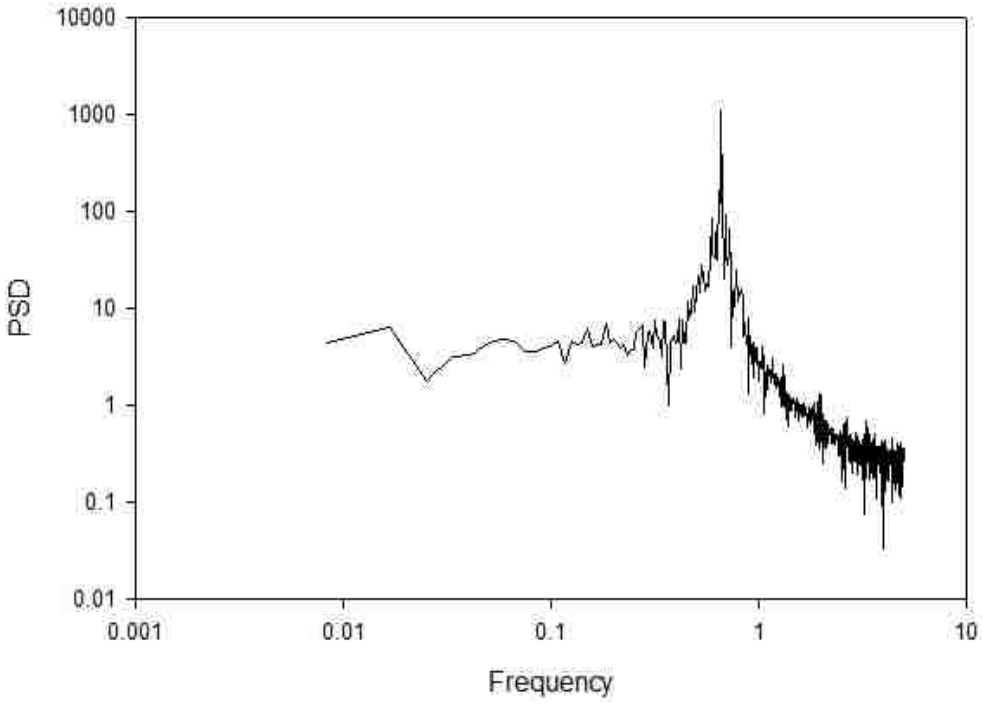

Figure 3.2 a) Steady, high amplitude vibrations and b) dominant peak frequency for plain cylinder during "synchronization" or "lock-in" in upper branch

Following validation experiments using the plain cylinder, cases 1 through 7 listed in Table 2.3 were performed to study the effect of decreasing roughness ratio. These experimental observations are discussed in detail as follows.

3.2 Effect of roughness ratio

Figure 3.3 shows the amplitude and frequency response of the cylinder for cases 1 through 7, with change in roughness ratio from 100% to 6.9%. In case 1, in which the rough strips are attached within the grooves of the cylinder, it is observed that the cylinder does not transition from VIV to galloping. The upper branch spans between $4.9 < U^* < 6.3$, where its amplitudes keep increasing and reach a maximum A^* value of 1. This trend is similar to the response of the plain cylinder in the upper branch, even though the value of amplitudes are consistently lower. As with the plain cylinder case, highest amplitudes are observed in this region that are characterized by stable displacement traces and dominant peak frequencies. The cylinder transitions into the lower branch between $6.37 < U^* < 9.94$, decreasing to an A^* value of 0.52. Beyond $U^* > 10.2$, the cylinder moves into an extended period of unsteady low amplitude oscillations, with A^* varying between 0.3 and 0.4, but does not desynchronize completely. During this period of unsteady behavior, the cylinder experiences a rise in f^* up to 1.2, varying ever so little around it. From around $U^* > 16.4$, f^* values start to gradually decrease back towards 1, but the cylinder does not transition into the galloping branch. Displacement and PSD plots for U^*=30 Hz within this region are shown in Figure 3.4. From the displacement trace, we can see random high and low amplitude oscillations without any periodicity. From the frequency spectrum, we do not observe a clear peak frequency.

Case 2 shows that the cylinder transitions from VIV to galloping at a U^* value of 16.4. The upper branch has a wider width compared to case 1, ranging from U^* value of 4.9 to 8.1. A^* values are similar to that of case 1, however, the upper branch sees a slower rate in decrease of A^* after reaching its peak for increasing U^*. Due to this, the upper branch starts to look like a straight line, slowly transitioning from having a negative slope to having no slope. This is also observed in case 3, after which the slope of the upper branch becomes positive and starts to rise for cases 4 through 7. Case 2 shows traces of a lower branch between $8.3 < U^* < 10.5$, representing a decrease in width compared to case 1. Even though the lower branch spans a smaller region, the A^* values are considerably higher as compared to case 1. Between $6.7 < U^* < 10.5$, A^* values for case 2 see an increase from 4% to 25% as compared to case 1. A similar decrease in width and increase in A^* values in the lower branch is noted for case 3 as well. Following the lower branch, case 2 enters into the transition zone between VIV and galloping. Figure 3.5 shows displacement traces and PSD plots for U^*=17 Hz (VIV-galloping transition), U^*=30 Hz (onset of galloping) and U^*=36 Hz (galloping). At the onset of galloping, the displacement trace shows periods of high steady oscillation amplitudes coupled with periods of small unsteady oscillation amplitudes. From the frequency spectrum, we can see the gradual increase in dominance of the peak frequency, followed by small peaks at higher harmonics. During galloping, A^* increases from 1.9 at U^*=16.4 to 2.3 at U^* = 20.7. The range for all experiments with galloping is limited to a U^* of 21.3 due to size limitations of the water tunnel and extreme flutter experienced at the free end of the cylinder. During galloping, there is a noticeable peak dominant frequency as seen in the PSD plot and smaller peaks at higher harmonics.

This is similar to the observations made by Park and Bernitsas [18]. The displacement trace during galloping shows steady large amplitude oscillations.

Case 3, with a roughness ratio of 20.3%, transitions from VIV to galloping at a U* value of 11.8, which is lower than what was observed for case 2. As with case 2, the length of the upper branch increases yet again, ranging from $5.1 < U^* < 9.1$. The A^* observed within the upper branch decreases at a rate of approximately 0.03/U*. In case 3, we can start to see the lower branch slowly disappearing with the cylinder moving into the transition zone soon after the upper branch, between $10.5 < U^* < 11.6$. During this zone, the A^* values fluctuate between 0.6 and 0.7, with displacement traces that show non-periodic oscillations. It was observed that this zone is particularly sensitive to effective thickness, showing an earlier transition to galloping with higher effective thickness. During this transition zone, f* rises from 1 to 1.2, and slowly drops back to unity at the onset of galloping, remaining relatively constant thereafter with increasing U^*. Beyond $U^* > 11.8$, the cylinder starts to gallop. A^* increases from 1.3 to 2.4 over $11.8 < U^* < 21.3$. Even though galloping occurs earlier for case 3 compared to case 2, A^* values during galloping response are relatively similar, indicating roughness ratio is still prevalent compared to H/D.

(a)

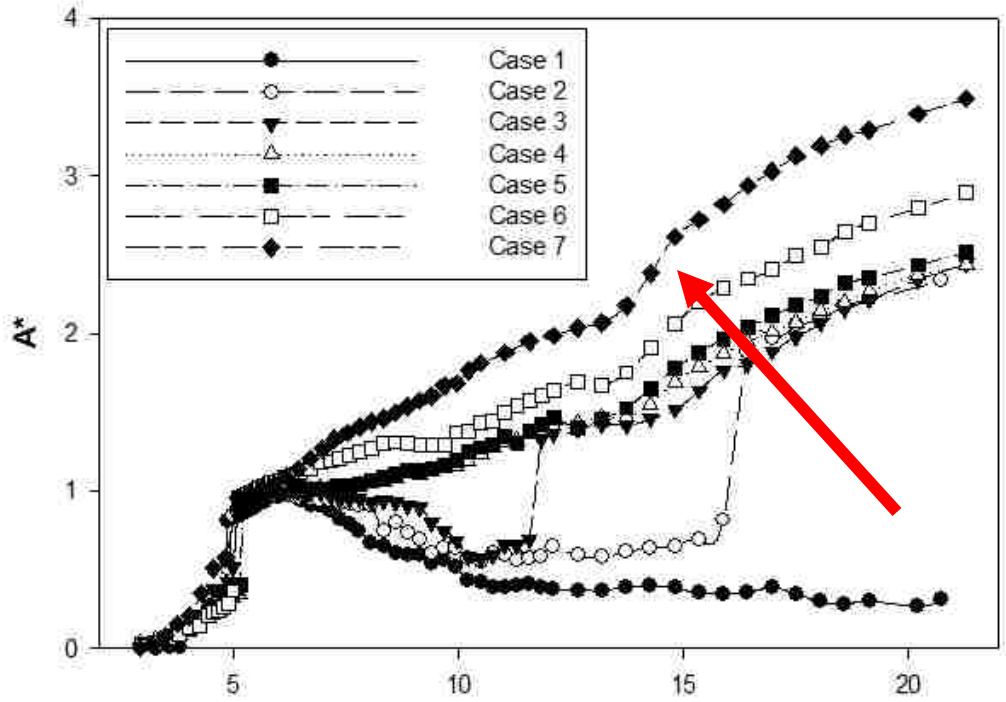

(b)

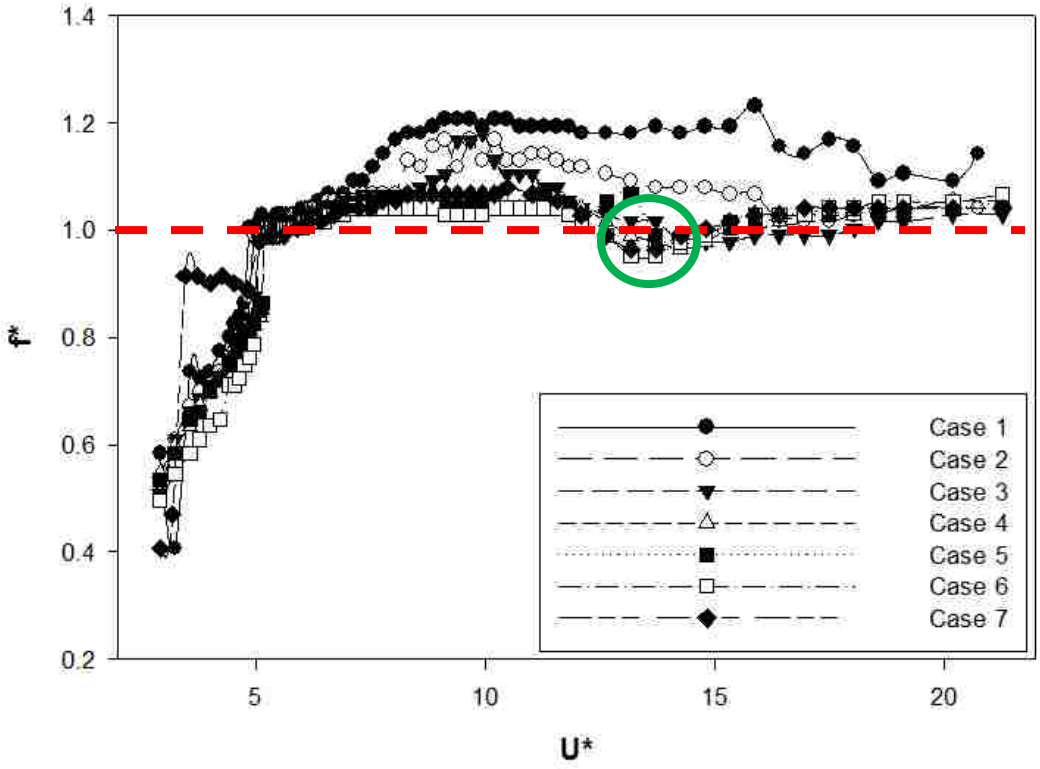

Figure 3.3 a) Amplitude and b) Frequency response for **RR = 100% to RR = 6.9%**

(a)

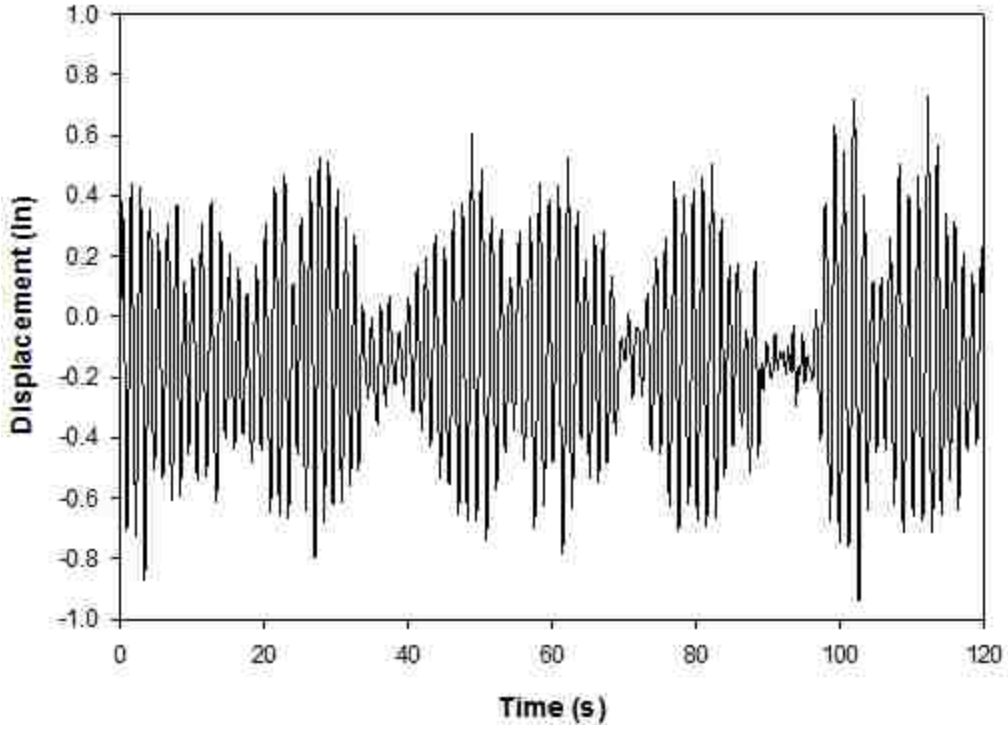

(b)

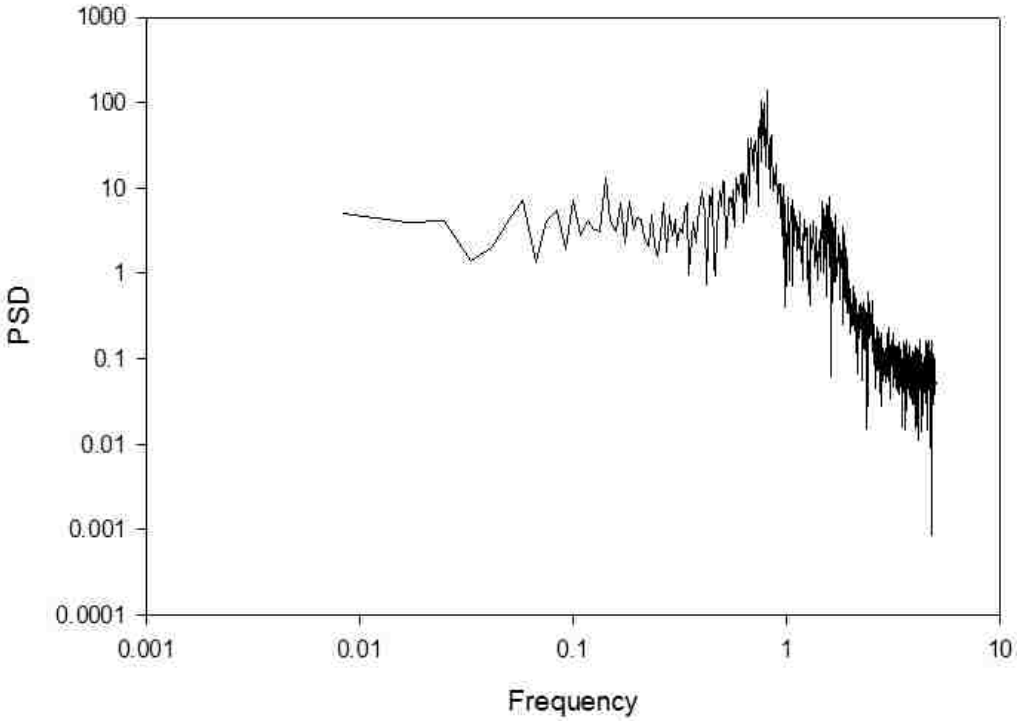

Figure 3.4 a) unsteady and fluctuating displacement trace, and b) lack of dominant frequency for **Case 1 with RR = 100% and H/D = 0.8%**

(a)

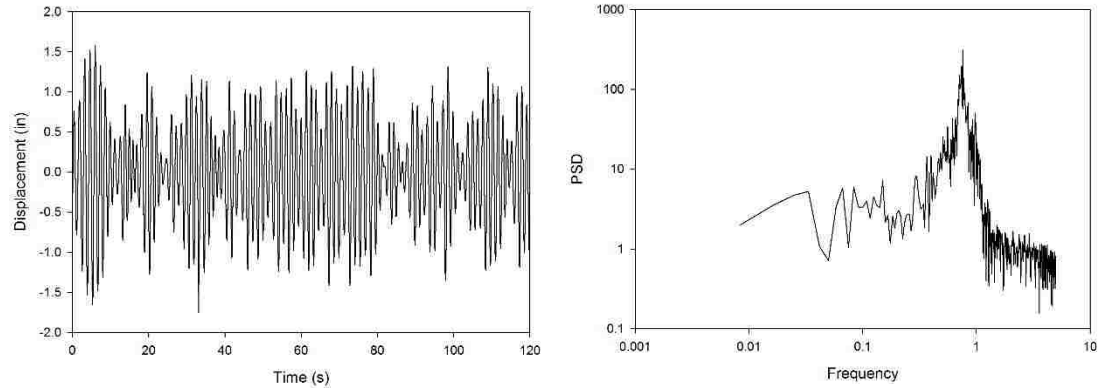

(b)

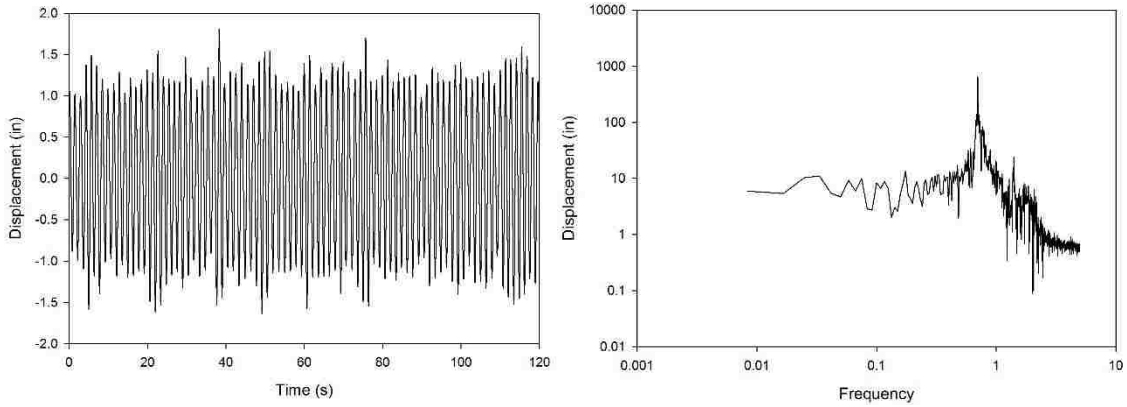

(c)

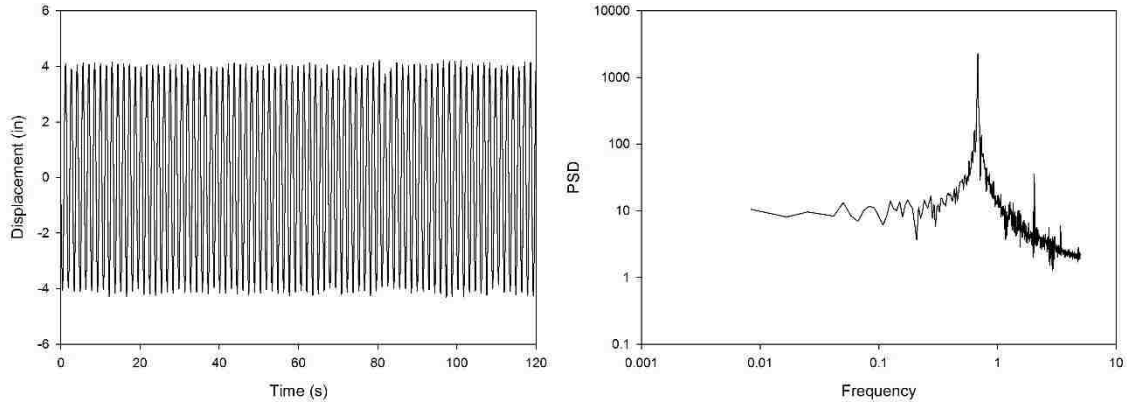

Figure 3.5 a) Transition zone, b) Onset of galloping, and c) Galloping for **Case 2, RR = 22.4% and H/D = 2.6%**

From cases 4 through 7, with roughness ratio decreasing from 18.6 % to 6.9 %, the lower branch ceases to exist in the response of the cylinder. Instead, VIV transitions directly from the upper branch to the galloping branch. Cases 4 and 5 show the upper branch occurring in relatively the same U^* region, between $5.2 < U^* < 8.6$. A^* values in this region fluctuate around 1.1, which coincides with the amplitudes for the plain cylinder case. A^* values for Cases 6 and 7 also coincide with the upper branch of the plain cylinder. However, the width of the upper branch for both these cases drops drastically. For both cases 6 and 7, the upper branch ranges from $5.1 < U^* < 6.2$. Since there is a direct jump to galloping for these lower roughness ratio cases, there is no clear transition region as was previously observed. Consequently, there is no longer a period of unsteady behavior in oscillations or fluctuations in frequencies as was observed in the transition zone at the onset of galloping for cases 2 and 3. The behavior of displacements and oscillation frequencies following the upper branch for case 4 is similar to the cylinder's response observed during galloping, as shown in Figure 3.5 c.

(a)

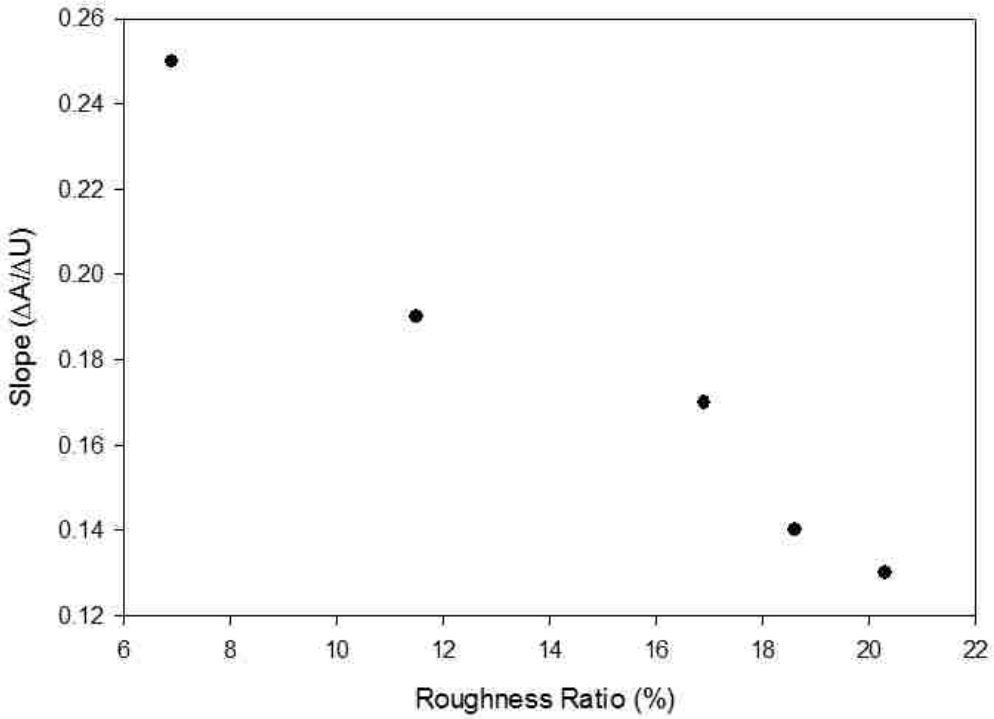

(b)

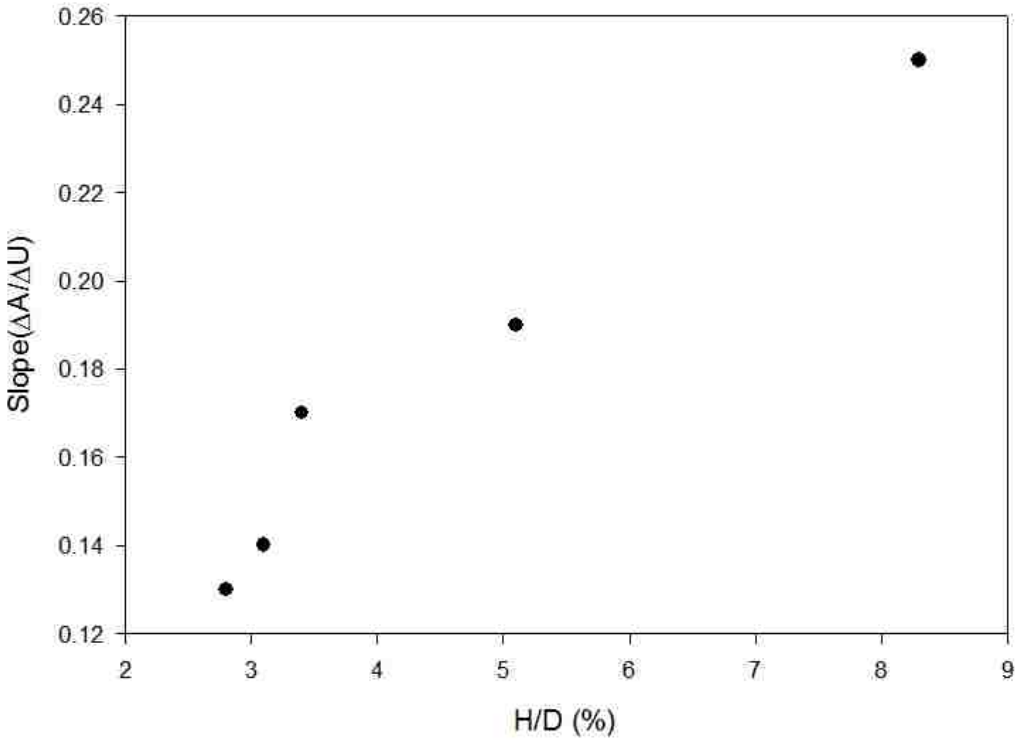

Figure 3.6 a) Increasing slope with decreasing RR, and b) Increasing slope with increasing H/D

For cases 4 through 7, there is a consistent increase in amplitudes across the entire range of U*, particularly with galloping amplitudes. The increased amplitudes are accompanied by a change in slope during the galloping branch for each case. Case 4 starts to gallop beyond U* > 8.9 and then shows an increased linear rate of galloping at a change of 0.14 in A^* per unit of U* between 13.2 < U* < 17, reaching a maximum A^* value of 2.4 over the experimental range of U*. Case 5 shows the galloping branch occurring in the same region as case 4. However, it shows a slightly higher rate of galloping at 0.16/U* between 13.2 < U* < 17, reaching a higher maximum A^* value of 2.5. Cases 6 and 7 transition into galloping beyond U* > 6.3, which is earlier than all the previously tested cases. Case 6 demonstrates a further increase in its slope for the comparable region, at 0.19/U* and reaches a maximum A^* value of 5.5. This maximum value is significantly higher than the previous case. Case 7, with an even lower roughness ratio of 6.9%, sees an increased rise in A^* of 0.25/U* and attains values as high as 6.6. From Figure 3.6, we can see that the change in slope within this region is inversely proportional to the increase in roughness ratio and directly proportional to the increase in H/D.

The oscillation frequencies for cases 4 through 7 show a decrease in f* value with a decrease in roughness ratios and remain steady around unity starting from the steady state vibration regime of the upper branch. Case 4 shows f* stays slightly higher than 1 beyond U* > 5.2, after which it briefly decreases to around 0.96 from 13.2 < U* < 14.8, following which it rises back up to unity with increasing U*. Case 5 shows similar trends, with f* values close to 1 beyond U* > 5.2, after which there is a drop to 0.96 from 13.7 < U* < 14.8, followed by a rise back to around unity. Case 6 depicts f* values closest to unity compared to other cases and experiences the lowest f* of 0.95 at U* of 13.7. Beyond that,

it shows a rise up to f* of 1.1. Case 7 shows f* values remain around 1.1 from 5.2 < U* < 11.6, after which there is a similar drop in value as with the other cases to 0.96 at U* of 13.2. After the decrease, Case 7 also increases up to unity and keeps getting closer to 1 with increasing U* values. The common observation between cases 4 to 7 is that the drop in f* occurs at the onset of the increase in slope of the galloping branch for each case. This is marked in Figure 3.3 b, where cases 3 through 7 see a drop in f* at approximately a U* value of 13.2. This trend was also observed in Auvil's work with varying strip thickness with smooth strips [34], suggesting that increasing H/D values show an increase in rate of galloping.

3.3 Effect of strip thickness at roughness ratio = 0%

Following the experiments with the rough P60 strips, test cases 8 through 14 with smooth strips were performed for similar H/D values as the rough strips. This presented a one to one comparison between the effect of smooth versus rough surfaces on the cylinder's VIV and galloping response. Case 8, with smooth strips at H/D = 0.8%, does not transition to galloping and eventually leads towards desynchronization. The upper branch of the cylinder spans between 5.0 < U* < 6.6, reaching a maximum *A** value of slightly greater than 1. As with the plain cylinder and P60 rough strip cases, the oscillation frequency remained approximately at 1 in the upper branch. The amplitudes in the upper branch for the smooth strip are consistently higher than those observed for case 1 with rough strips at H/D = 0.8%. Similar to the rough strips, steady vibrational amplitudes from the displacement trace along with peak dominant frequencies are observed during this period. The lower branch for case 8 occurs between 6.7 < U* < 10.8, with *A** values dropping from 0.95 to 0.53. Comparisons between case 1 and 8 show maximum difference between the

smooth and rough strips during the lower branch, with the smooth strips consistently achieving higher *A** values over the period. Around U* = 12.1, the cylinder's response enters into an extended period of random unsteady fluctuations in amplitude oscillations, similar to what was observed with case 1 with the rough strips. There is an overlap between *A** values for case 1 and 8 from 12.1 < U* < 15.3. Following that, case 8 shows that the cylinder heads towards desynchronization, dropping to *A** of 0.08 at U* = 20.7. Figure 3.8 shows the displacement trace and PSD plots at a U* value of 19.1. From this, we can see that the oscillations are sporadic and are lower in magnitude compared to what was observed for the P60 strip in case 1. Furthermore, no clear peaks are seen from the frequency spectrum which result in fluctuations in f* values in this region. From U* = 6.7, f* continues to rise from 1 to 1.2, after which it rises further to 1.3 at U* = 18.6, which is the highest value of f* recorded from all the 14 experimental cases that were performed.

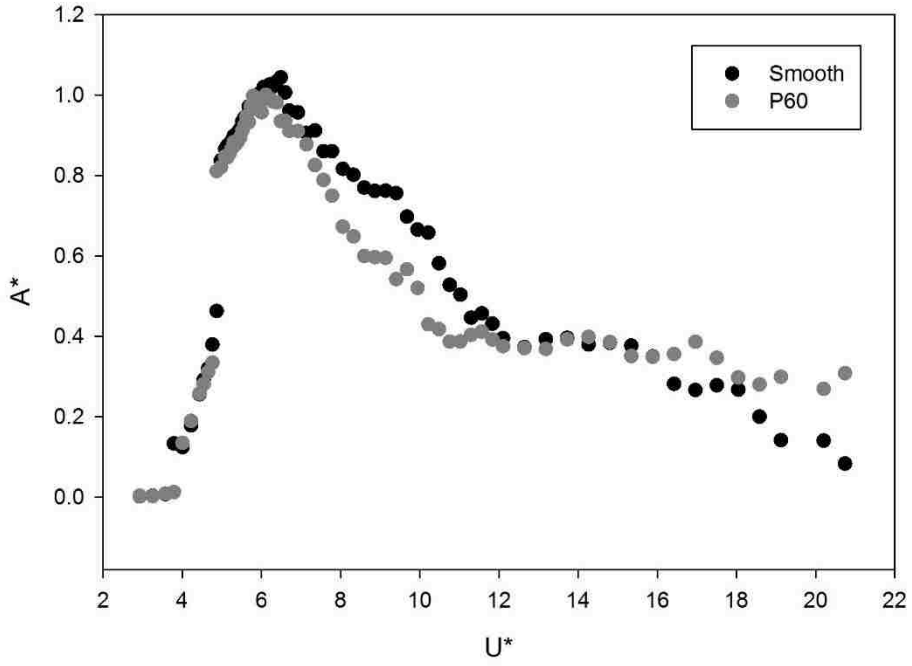

Figure 3.7 Comparison of amplitude response between **Case 1 and Case 8 (H/D ~ 0.8%)**

(a)

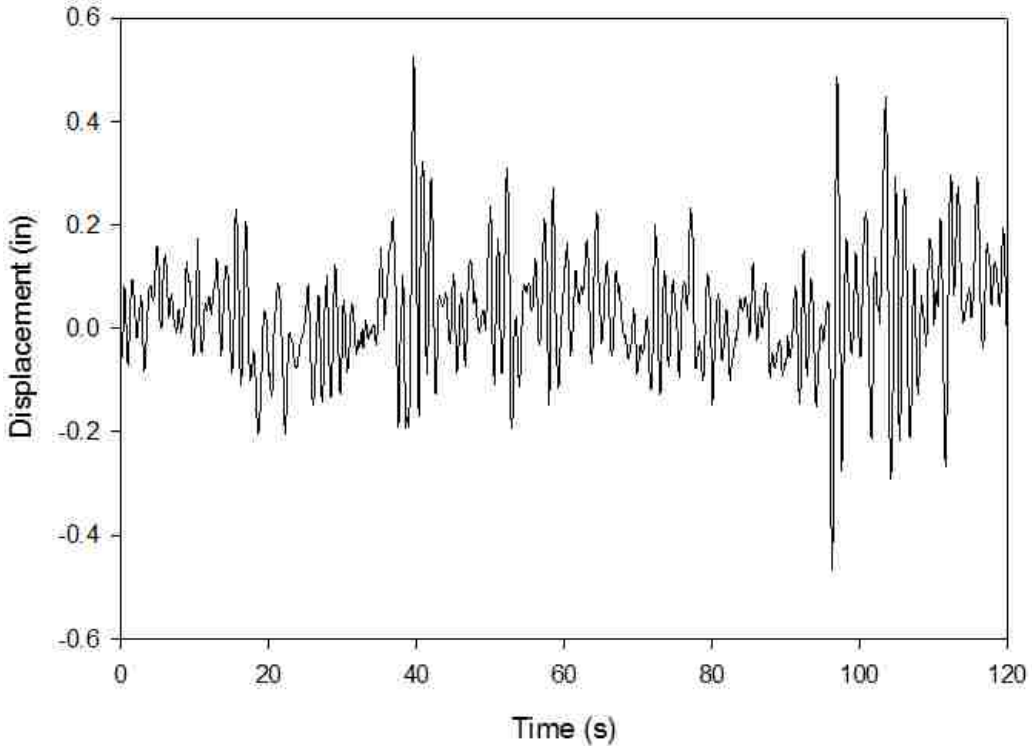

(b)

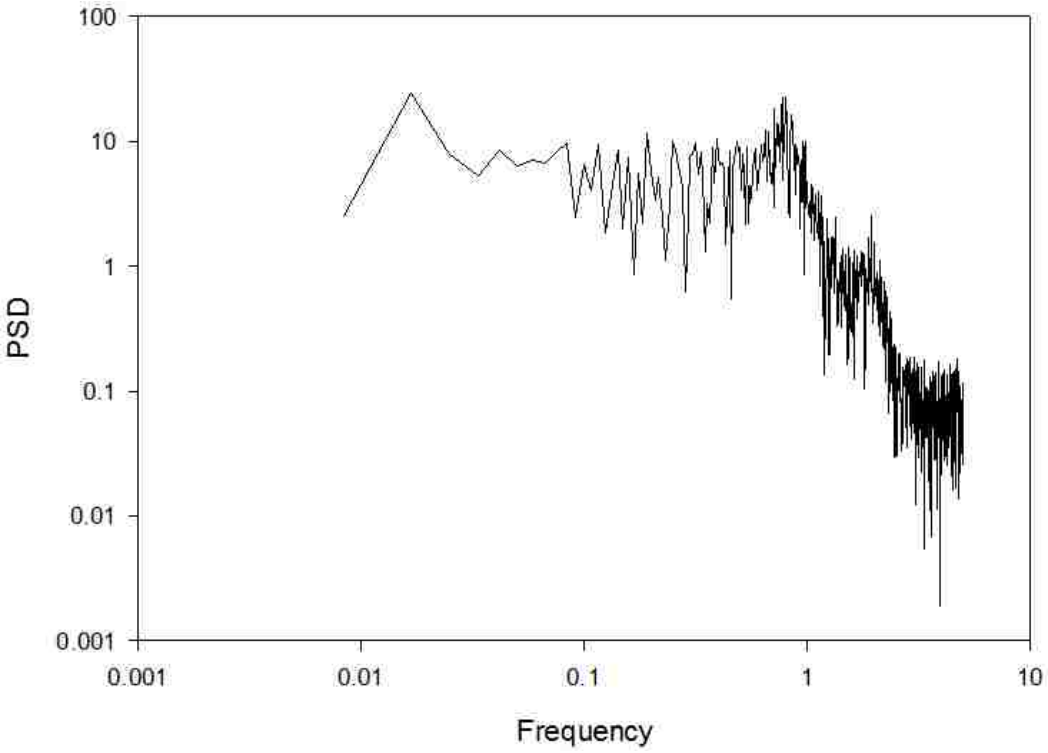

Figure 3.8 a) Displacement trace and b) PSD response of **Case 8 at U*=19.1 for H/D = 0.8%**

(a)

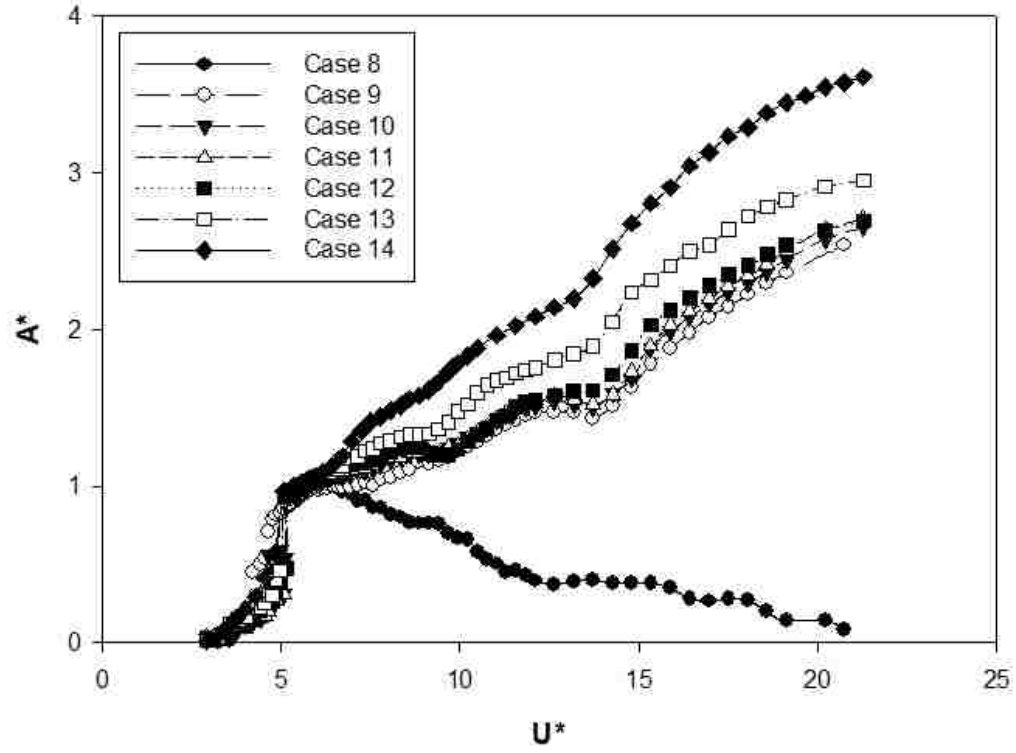

(b)

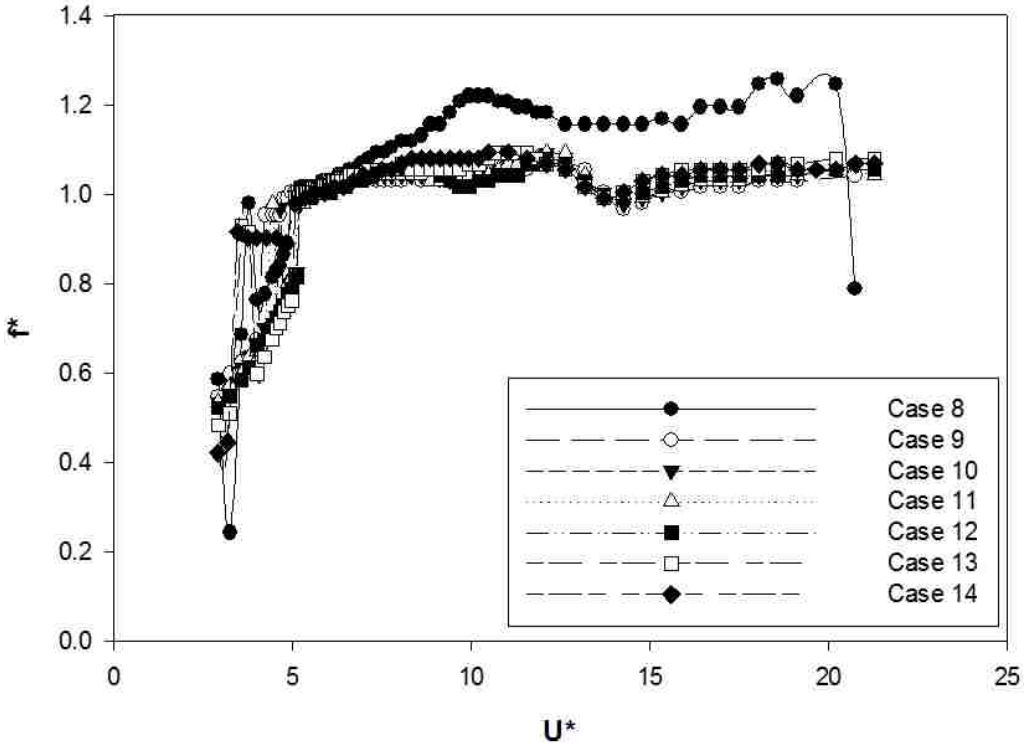

Figure 3.9 a) Amplitude response and b) Frequency response of **Cases 8 – 14**

From cases 9 through 14, with increasing H/D values from 2.4% to 8.2% for the smooth strips, there is no distinguishable lower branch, with the cylinder transitioning directly from the upper branch to the galloping branch. Furthermore, with increasing H/D values, the amplitude of vibrations are seen to increase over the entire range of U* for all cases. Case 9 shows the onset of galloping starting around U* > 8.1, which is higher than other proceeding cases. This indicates that the width of the upper branch starts to decrease with higher H/D values, similar to what was observed with decreasing roughness ratio from cases 1 through 7. At U* of 13.7, there is an increase in the rate of galloping at 0.16/U*, reaching a maximum A^* value of 2.5 at U* = 20.7. Cases 10, 11 and 12, with incremental changes in H/D from 2.7% to 3.3%, show a very similar rate of increase in slope between 13.7 < U* < 19.1, of approximately 0.17/U*. Case 13, with a moderate increase of H/D to 4.9%, shows distinctively higher A^* values compared to previous cases from 9-12, reaching a maximum A^* of 2.9. However, it still shows a rate of increase at 0.17/U* beyond U* > 13.7. Case 14, with a bigger step over to H/D of 8.2%, shows an increase in both A^* values as well as the rate of galloping. Maximum A^* of 3.6 is reached at an increased rate of 0.2/U*. The oscillation frequencies for the smooth strip cases, with the exception of case 8, remain stable starting from the upper branch regime. Cases 9 through 12 show steady f* values of approximately 1 until U* = 10.5. After this point, there is a slight increase in f* to 1.1 between 10.2 < U* < 12.6. This is followed by a drop to approximately 0.97 at a U* of 14.2 and then an increase in f* back up to unity for following U* values. Cases 13 and 14 experience the drop in f* at a lower U* of 13.7, after which they also remain constant around unity. For the smooth strip cases, it is once again observed that the drop in f* occurs around the same period as the change in slope of the galloping branch. This agrees with

Auvil's findings from the effect of thickness using smooth strips [34], where he showed the increase rate of galloping was closely associated with a drop in f* followed by a rise back up to unity.

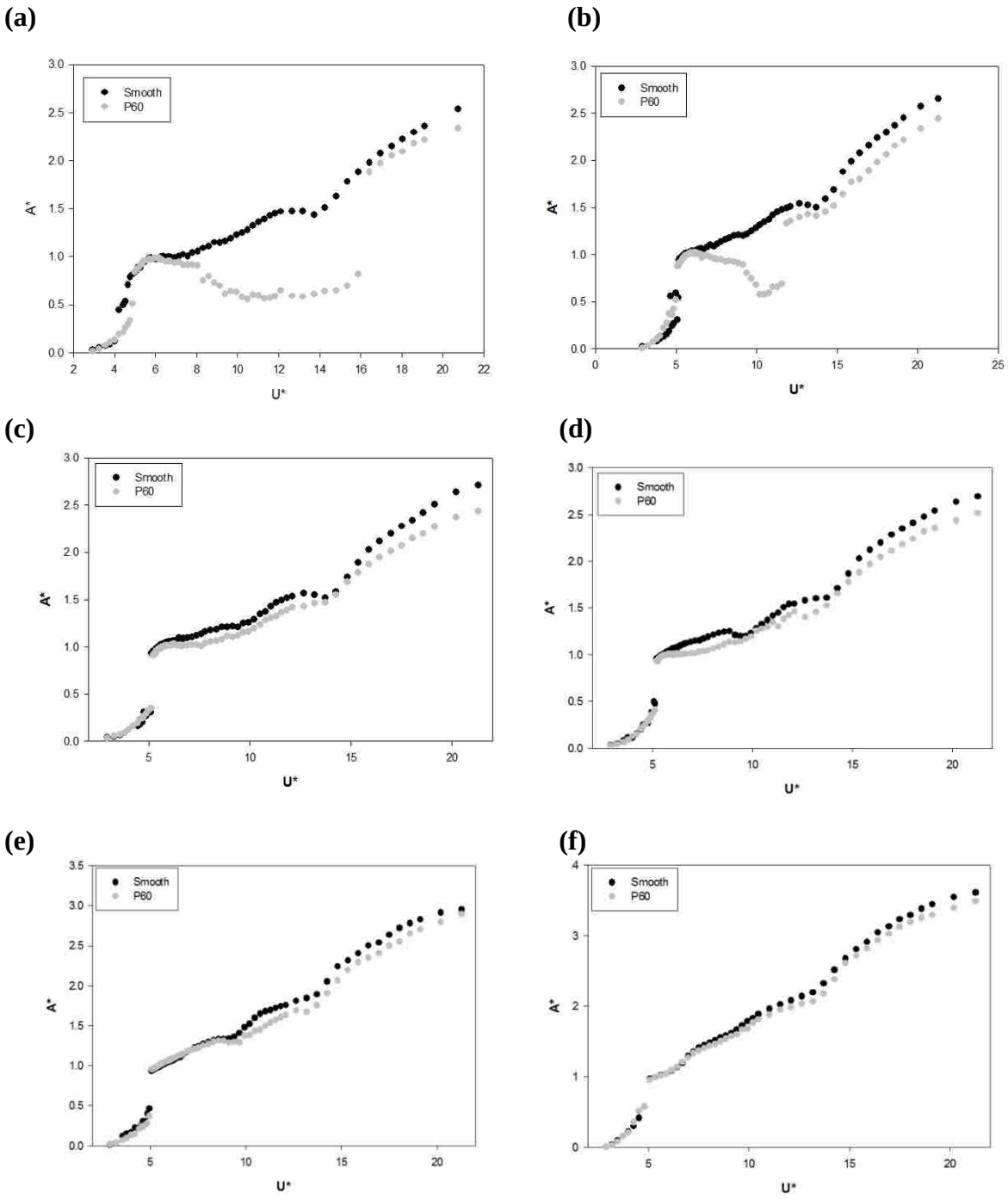

Figure 3.10 Comparison of amplitude response **for a) H/D=2.4%, b) H/D=2.7%, c) H/D=2.9%, d) H/D=3.3%, e) H/D=4.9%, and f) H/D=8.2%**

Figure 3.10 (a)-(f) show comparisons between each case of the smooth and rough strips based on their respective H/D values. We can see that both surfaces behave differently at low H/D values, but gradually start to demonstrate the same response across the entire range of U* at higher values of H/D. For cases 1-7, high H/D values correspond to lower roughness ratios. Comparisons between case 2 and case 9 show that there is a remarkable disparity between the response of the cylinder from $6.9 < U^* < 15.9$ for smooth versus rough strips. Case 9 shows a direct transition to galloping, whereas case 2 shows an extended period of fluctuating low amplitude oscillations. Within this region, the cylinder configuration for Case 9 demonstrates steady, high amplitude oscillations with dominant peak frequencies (see Figure 3.5c). However, in Case 2, there are fluctuations in the displacement trace and frequency in this region, showing no clear dominant peak frequency. In the range $16.4 < U^* < 20.7$, case 2 transitions to galloping, however with slightly decreased amplitudes compared to case 9. In this region, the percent difference between A^* values for smooth and rough surfaces keeps growing with increasing U* values, reaching a maximum difference of 7.9%. In this region, the amplitudes within the galloping branch for smooth strips increases at a faster rate of 0.14/U* compared to 0.11/U* of case 2. Both these trends are observable when comparing cases 3 and 10, 4 and 11, and 5 and 12. Analysis of cases 3 and 10 shows coinciding values of A^* at U* of 13.7. In this region, A^* for the smooth strip drops to 1.5, and A^* for the rough strip drops to 1.4, giving a percent difference of only 6%. In this region, f* values are seen to drop to their lowest values for both cases respectively. As discussed earlier, a drop in f* value was associated with a change in the slope of the galloping branch. Adding on to this idea, it is noticed that before there is a change in slope during galloping for either surface, there is a

decrease in the difference between A^* values which also corresponds to a decrease in f*. This trend is observed in all comparison cases starting from case 3 with 10 to case 7 with 14. Comparisons between case 4 and 11 show that the disparity with A^* values between rough and smooth strips starts to decrease, with case 4 showing a direct transition to galloping from the upper branch for the rough strips. With increasing values of H/D and decreasing values of roughness ratio for comparison cases 5 with 12, 6 with 13 and 7 with 14, we can see a similar response in A^* and f* values. All comparison cases from here on show similar steady vibrational amplitudes and dominant oscillation frequencies within the galloping branch. Due to this, it is observed that the percent difference for A^* values starts to decrease slowly over the U^* range. Average percent difference between case 5 and 12, 6 and 13 and 7 and 14 in the range of $5.2 < U^* < 13.7$ is 6.0%, 3.6 % and 3.1% respectively. Similarly, the average percent difference between case 5 and 12, 6 and 13 and 7 and 14 in the range of $13.7 < U^* < 21.3$ is 6.5%, 5.4%, and 3.8%. Evidently, the gap between smooth and rough strips start to close in with increasing H/D and decreasing roughness ratio, resulting in similar trends in VIV and galloping response. Figure 3.11 demonstrates this trend through the decrease in difference of A^* values between cases 5 and 12, 6 and 13 and 7 and 14 beyond the steady regime period of vibration.

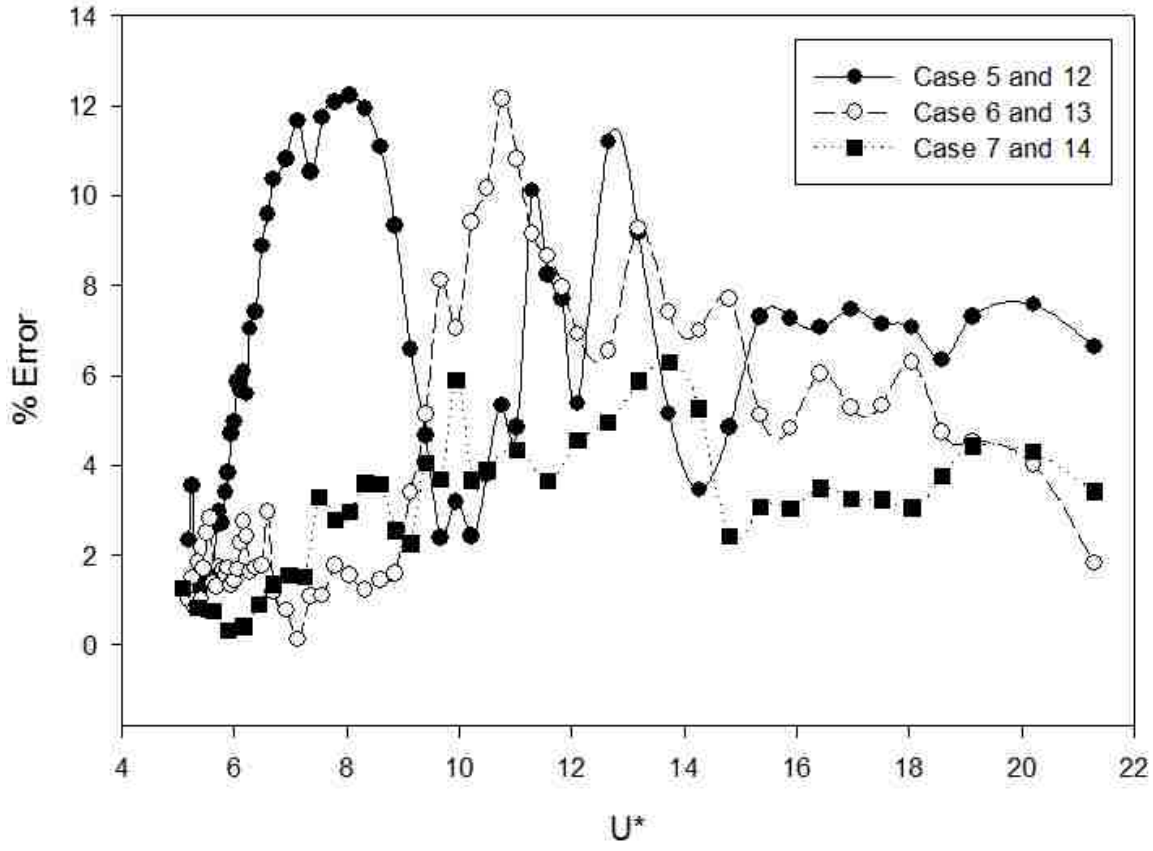

Figure 3.11 Comparison of % error difference for $U^* > 5$

4 Conclusions

Experimental cases 1 through 7 examined the effect of decreasing roughness ratio on the cylinder's VIV and galloping response. Experimental cases 8 through 14 studied the effect of smooth strips at similar H/D ratios as cases 1 through 7 in order to draw comparisons between both types of surfaces on the cylinder's VIV and galloping response. We summarize the main findings from the experimental results as follows:

- There exists a lower threshold of thickness below which galloping does not take place, irrespective of the type of surface attached to the cylinder, i.e., smooth or rough. At H/D of 0.8%, cases 1 and 8 showed that neither the rough or smooth strips were able to excite the cylinder into the galloping branch.
- The effect of roughness on the surface of the cylinder is prevalent at higher roughness ratios and lower H/D values. Cases 2 through 4 showed reduced VIV and galloping amplitudes in the cylinder's response when using rough strips versus smooth strips. At a roughness ratio of 22.4%, the cylinder underwent diminished amplitudes that fluctuated between $0.5 < A^* < 0.6$ in the range of $9.4 < U^* < 15.4$. At this same period, the cylinder attached with smooth strips galloped, increasing from A^* of 1.2 to 1.8.
- The onset of galloping shifts to lower values of U^* with an increase in thickness and decrease in roughness ratio. Case 3, with a H/D of 2.8%, showed that it was able to gallop at a U^* of 11.8 whereas case 2, with H/D of 2.6%, transitioned into galloping at U^* of 16.4. This holds true for smooth strips as well, as shown by the earlier transition into galloping from cases 9 through 14 with increasing thickness of strips used.
- The effect of strip surface on FIM response weakens with a decrease in roughness ratio. Cases 5 through 7 show that with a reduction in roughness ratio, the percent difference

in galloping amplitudes between smooth and rough strips reduces from an average error of 6.0% to 3.1% in between $5.2 < U^* < 13.7$.

- Both rough and smooth strips demonstrated an increase in the rate of galloping observed through the change of slope of the amplitude response. This phenomenon occurred at the same U^* value of 13.7 for both smooth and rough strips for H/D of 3.3%, 4.9%, and 8.2%.
- For all cases tested, except cases 1 and 8, the VIV regime and galloping branch demonstrated steady high amplitude vibrations that corresponded to a f* of 1 starting from the upper branch of the cylinder's response.
- There exists an upper threshold of thickness, around which the impact of the type of surface on the cylinder's response to VIV and galloping becomes negligible. At H/D of 8.2%, comparisons between case 7 and 14 show clear overlap in galloping amplitudes across the tested U^* range, with lowest percent error value of 3.4% averaged over $5.2<U^*<21.3$.
- At higher H/D values, the parameter that holds the strongest influence on the augmentation of VIV and galloping amplitudes is thickness. Cases 1 through 14 all show change in oscillation behavior with incremental changes in thickness, validating how sensitive the cylinder's response is to strip thickness compared to other experimental parameters.

References

1. Naudascher, E. and D. Rockwell, *Flow-Induced Vibrations*. 1994: Dover Publications.
2. Morgenthal, G., *Fluid Structure Interaction in Bluff-body Aerodynamics and Long-span Bridge Design: Phenomena and Methods*. 2000: University of Cambridge, Department of Engineering Cambridge.
3. Khalak, A. and C.H. Williamson, *Motions, forces and mode transitions in vortex-induced vibrations at low mass-damping.* Journal of fluids and Structures, 1999. **13**(7-8): p. 813-851.
4. Zdravkovich, M.M., *Flow around Circular Cylinders; Volume1: Fundementals*. Vol. 1. 1997: Oxford university press.
5. Williamson, C.H. and A. Roshko, *Vortex formation in the wake of an oscillating cylinder.* Journal of fluids and structures, 1988. **2**(4): p. 355-381.
6. Alonso, G., E. Valero, and J. Meseguer, *An analysis on the dependence on cross section geometry of galloping stability of two-dimensional bodies having either biconvex or rhomboidal cross sections.* European Journal of Mechanics-B/Fluids, 2009. **28**(2): p. 328-334.
7. Alonso, G., et al., *On the galloping instability of two-dimensional bodies having elliptical cross-sections.* Journal of Wind Engineering and Industrial Aerodynamics, 2010. **98**(8-9): p. 438-448.
8. Bernitsas, M.M., et al., *VIVACE (Vortex Induced Vibration Aquatic Clean Energy): A new concept in generation of clean and renewable energy from fluid flow.* Journal of offshore mechanics and Arctic engineering, 2008. **130**(4): p. 041101.

9. Sarpkaya, T., *Vortex-induced oscillations: a selective review.* Journal of applied mechanics, 1979. **46**(2): p. 241-258.

10. Sarpkaya, T., *A critical review of the intrinsic nature of vortex-induced vibrations.* Journal of fluids and structures, 2004. **19**(4): p. 389-447.

11. Williamson, C. and R. Govardhan, *Vortex-induced vibrations.* Annu. Rev. Fluid Mech., 2004. **36**: p. 413-455.

12. Bearman, P., *Circular cylinder wakes and vortex-induced vibrations.* Journal of Fluids and Structures, 2011. **27**(5-6): p. 648-658.

13. Khalak, A. and C. Williamson, *Fluid forces and dynamics of a hydroelastic structure with very low mass and damping.* Journal of Fluids and Structures, 1997. **11**(8): p. 973-982.

14. Lee, J. and M. Bernitsas, *High-damping, high-Reynolds VIV tests for energy harnessing using the VIVACE converter.* Ocean Engineering, 2011. **38**(16): p. 1697-1712.

15. Raghavan, K. and M. Bernitsas, *Experimental investigation of Reynolds number effect on vortex induced vibration of rigid circular cylinder on elastic supports.* Ocean Engineering, 2011. **38**(5-6): p. 719-731.

16. Assi, G.R. and P.W. Bearman, *Transverse galloping of circular cylinders fitted with solid and slotted splitter plates.* Journal of Fluids and Structures, 2015. **54**: p. 263-280.

17. Chang, C.-C.J., R.A. Kumar, and M.M. Bernitsas, *VIV and galloping of single circular cylinder with surface roughness at $3.0\times 10^4 \leq Re \leq 1.2\times 10^5$.* Ocean Engineering, 2011. **38**(16): p. 1713-1732.

18. Park, H., R.A. Kumar, and M.M. Bernitsas, *Enhancement of flow-induced motion of rigid circular cylinder on springs by localized surface roughness at $3\times104\leq Re\leq1.2\times105$.* Ocean Engineering, 2013. **72**(0): p. 403-415.

19. Nemes, A., et al., *The interaction between flow-induced vibration mechanisms of a square cylinder with varying angles of attack.* Journal of Fluid Mechanics, 2012. **710**: p. 102-130.

20. Mannini, C., A. Marra, and G. Bartoli, *VIV–galloping instability of rectangular cylinders: review and new experiments.* Journal of Wind Engineering and Industrial Aerodynamics, 2014. **132**: p. 109-124.

21. Weaver, D. and I. Veljkovic, *Vortex shedding and galloping of open semi-circular and parabolic cylinders in cross-flow.* Journal of fluids and structures, 2005. **21**(1): p. 65-74.

22. Novak, M., H. Tanaka, and A.G. Davenport, *Vibration of towers due to galloping of iced cables.* Journal of the Engineering Mechanics Division, 1978. **104**(2): p. 457-473.

23. Bokaian, A. and F. Geoola, *Flow-induced vibrations of marine risers.* Journal of Waterway, Port, Coastal, and Ocean Engineering, 1987. **113**(1): p. 22-38.

24. Dhanak, M.R. and N.I. Xiros, *Springer Handbook of Ocean Engineering*. 2016: Springer.

25. Jacobson, P.T., et al., *Assssment and Mapping of the Riverine Hydrokinetic Resource in the Continental United States*. 2012, Electric Power Research Institute.

26. Zdravkovich, M., *Review and classification of various aerodynamic and hydrodynamic means for suppressing vortex shedding.* Journal of Wind Engineering and Industrial Aerodynamics, 1981. **7**(2): p. 145-189.

27. Zdravkovich, M. and J. Volk, *Effect of shroud geometry on the pressure distributed around a circular cylinder.* Journal of Sound and Vibration, 1972. **20**(4): p. 451-455.

28. Sui, J., et al., *VIV suppression for a large mass-damping cylinder attached with helical strakes.* Journal of Fluids and Structures, 2016. **62**: p. 125-146.

29. Park, H., R.A. Kumar, and M.M. Bernitsas, *Suppression of vortex-induced vibrations of rigid circular cylinder on springs by localized surface roughness at* $3\times 10^4 \leq Re \leq 1.2\times 10^5$. Ocean Engineering, 2016. **111**: p. 218-233.

30. Nakagawa, K. *An experimental investigation of aerodynamic instability of circular cylindersat supercritical Reynolds numbers*. in *Proceedings of the 9th Japan, Congress Applied Mechanics*. 1959. Tokyo.

31. Mahrenholtz, O. and H. Bardowicks, *Aeroelastic problems at masts and chimneys.* Journal of Wind Engineering and Industrial Aerodynamics, 1979. **4**(3-4): p. 261-272.

32. Gartshore, I., J. Khanna, and S. Laccinole, *The effectiveness of vortex spoilers on a circular cylinder in smooth and turbulent flow*, in *Wind Engineering*. 1980, Elsevier. p. 1371-1379.

33. Vinod, A. and A. Banerjee, *Surface protrusion based mechanisms of augmenting energy extraction from vibrating cylinders at Reynolds number* $3\times 10^3–3\times 10^4$. Journal of Renewable and Sustainable Energy, 2014. **6**(6): p. 063106.

34. Auvil, A., *Effects of Strip thickness and damping on flow-induced motions of a circular cylinder*, in *Department of Mechanical Engineering*. 2017, Lehigh University.

Appendix

A. LVDT Assembly and Electronics

The LVDT assembly consists of the core rod and LVDT body (cylinder). The model of LVDT used for the experiments was purchased from Macro Sensors, which is a subsidiary company of TE Connectivity. The bore diameter of the LVDT body is 0.235,'' and the core rod diameter is 0.188''. As a result, the clearance between the core rod and inner surface of the LVDT is only 0.188''. Threaded rods of size #4-40 were used, which proved to work well with the amount of clearance available. The small diameter of the rods allowed them to be flexible enough so that they could be pulled taut and prevent sagging inside the LVDT body. It would be worthwhile to check to see if there is a core rod smaller in diameter that could be used for the same LVDT body available in the market as it would increase the clearance and reduce complications of friction/scraping. Figure A.1 shows the cross section and side view of the cylinder-core rod system.

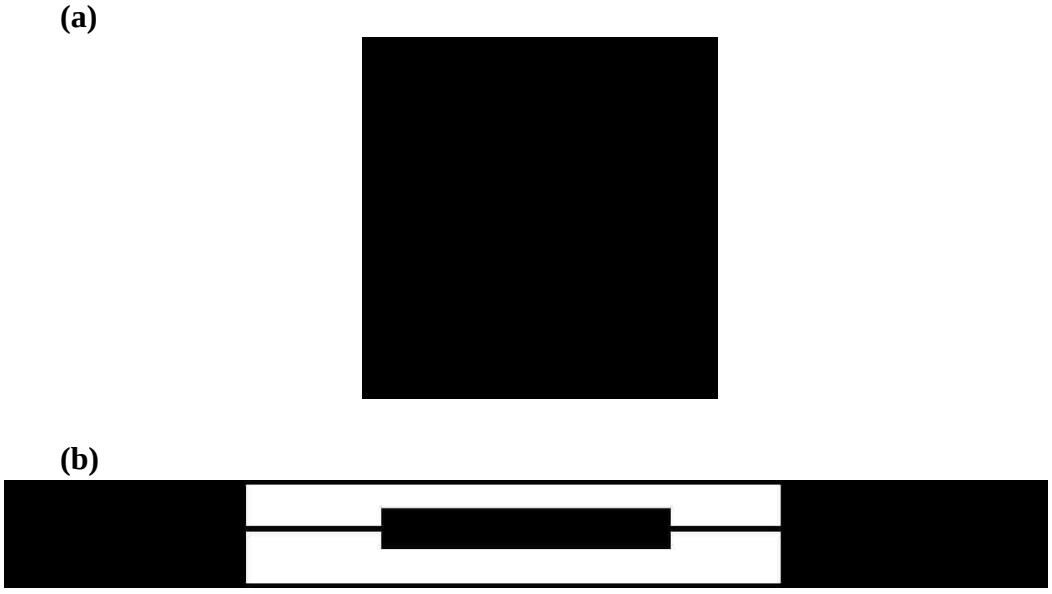

Figure A.1 a) Cross section showing theoretical clearance and b) side view of LVDT system

A 3.3 A, 24 VCD National Instruments power supply model PS-14 was used to power the LVDT. The LVDT is wired to the power supply as well as the DAQ. The DAQ has 8 analog input terminals and an output terminal for USB. Figure A.2 provides the overall wiring system connecting the power supply, LVDT, DAQ, and CPU.

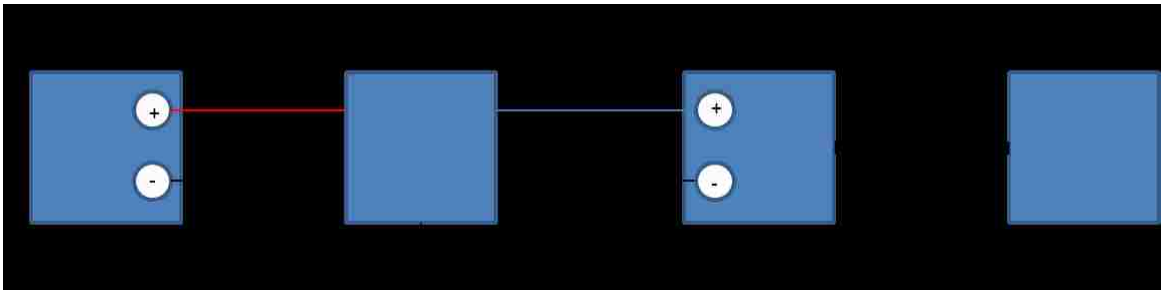

Figure A.2 Wiring Diagram for DAQ system

B. Data Acquisition

Figure D.1 provides the block diagram of the LabVIEW VI script that was used to acquire data. In order to link the USB-6003 DAQ board, the DAQ Assistant command was used in LabVIEW. The range of the voltage readings from the DAQ board is from -10 V to + 10 V. From the linearity relationship with a slope of 2, the displacement range is – 20 in to + 20 in. The sampling time for each experiment was 2 minutes and was collected at a rate of 10 Hz. This corresponds to reading 1200 samples at 10 samples per second.

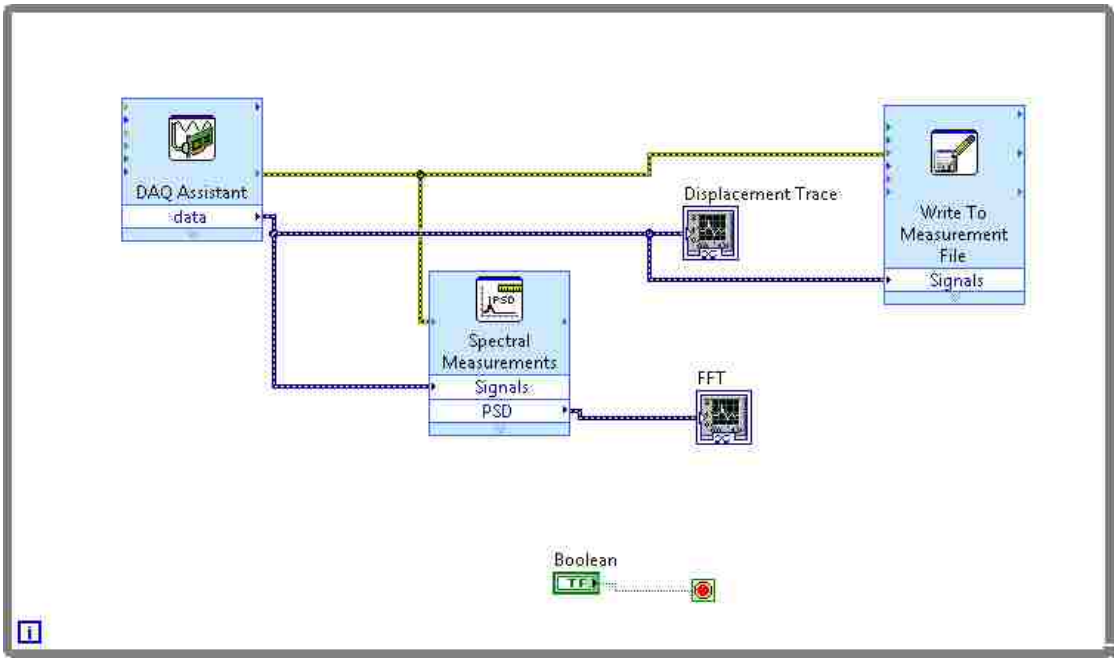

Figure B.1 LabVIEW VI Block Diagram

C. MATLAB Scripts

C.1 Displacement Trace Processing

```
clc;
clear;
close all;

disp = xlsread('11_9hz','B23:B1222');
% disp = disp' - 11.18673;  % 11.02144
% disp = disp' - 11.17649;  % 11.02144
% disp = disp' - 11.15312;  % 11.02144
disp = disp' - 11.14882;

num_of_files = numel(disp);
time = 0.1:0.1:num_of_files/10;

% Plot displacement trace
plot(time,disp,'-')

% Plot frequency spectrum
[F,X] = FFT(disp,time);
figure
loglog(F,X)

Fplot = F';
Xplot = X';
dispplot = disp';
timeplot = time';

amplitudes = finding_amplitudes(disp);

sorted_amplitudes = sorting(amplitudes);

total_average = sum(sorted_amplitudes)/length(sorted_amplitudes)

top_10 = 0.1*length(sorted_amplitudes);

top_20 = 0.2*length(sorted_amplitudes);

for z = 1:top_10
    filter_10(z) = sorted_amplitudes(z);
end

for y = 1:top_20
    filter_20(y) = sorted_amplitudes(z);
end

top_10_average = sum(filter_10)/length(filter_10)

top_20_average = sum(filter_20)/length(filter_20)
```

```
%%% Power Calculation ------------------------------------------------
---

dispm = disp*0.0254;

vel = zeros(1,length(time));

for i=2:length(time)
    vel(i) = (dispm(i)-dispm(i-1))/(time(i)-time(i-1));
end

save('results.mat')
Arms = rms(amplitudes)
Drms = rms(disp);
Vrmssq = (rms(vel))^2
rmsdata = [top_10_average,Arms,Drms,Vrmssq];
xlswrite('RMS Values.xlsx',rmsdata)
```

C.2 Damping Tests

```
clc;
clear;
figure
disp = xlsread('dampingtest,'B23:B322');
disp = disp';
disp = disp - 11.14882;

numtime = numel(disp);

for j=1:numtime
%     disp(j) = (first-Z(1,j))*0.0258;
    time(j)=(j-1)/10;
end

plot(time,disp,'-')
% title('Displacement History')
xlabel('Time (s)')
ylabel('Displacement (in)')

timeplot = time';
dispplot = disp';

spring_k = 84.4;
mass = 4.79;
n=length(disp);

for start=1:n
    if disp(1,start)~= disp(1,start+1)
        break;
    end
end
if disp(1,start+1) >= disp(1,start)
```

```
    direction=1;       % If direction is 1 then curve starts going up
ward
else
    if disp(1,start+1) < disp(1,start)
        direction=2;   % If direction is 2 then curve starts going
downward
    end
end
% record = zeros(1,101);
%record(1) = disp(1);
p=1;
if direction ==1      % Curve starts Going up from begining
    flag=1;
    for i=start:n-1
        if flag==1    % It is going up
            if disp(1,i+1) < disp(1,i)
            record(p)=disp(1,i);
            p=p+1;
            flag=0;
            end
        end
        if flag==0    % It is going down
            if disp(1,i+1) > disp(1,i)
               record(p)=disp(1,i);
               p=p+1;
               flag=1;
            end
        end
    end
end
if direction ==2      % Curve starts Going Down from begining
    flag=0;

    for i=start:n-1

        if flag==0    % It is going down

            if disp(1,i+1) > disp(1,i)
            record(p)=disp(1,i);
            p=p+1;
            flag=1;
            end

        end

        if flag==1    % It is going up
            if disp(1,i+1) < disp(1,i)
               record(p)=disp(1,i);
               p=p+1;
               flag=0;
            end
        end
    end

end
%
```

```
%record = record(2:length(record));
% using first peak
k = 1;
zeta = zeros(24,1);
for n = 1:24
    decc = (1/n)*log(record(1)/record(2*n+1));

    zeta(k)=decc/sqrt((4*pi*pi)+(decc)^2);

    C(k)=2*zeta(k)*sqrt(spring_k*mass);
    k=k+1;

end


avg_damping=mean(C)
avg_zeta=mean(zeta)
```

Vita

Kumar Swagat was born on October 3, 1994, in Odisha, India. He received his Bachelor of Science degree in Mechanical Engineering from Lehigh University in May 2017. During his undergraduate career, he completed engineering internships with AES Corporation and The Linde Group. He received the presidential scholarship from Lehigh and joined the Turbulent Flows Laboratory in June 2017. Kumar graduated with a Master of Science degree in Mechanical Engineering in May 2018.